Subsonic and intersonic shear rupture of weak planes with a velocity weakening cohesive zone

O. Samudrala
Graduate Aeronautical Laboratories, California Institute of Technology, Pasadena, California, USA

Y. Huang
Department of Mechanical and Industrial Engineering, University of Illinois at Urbana-Champaign, Urbana, Illinois, USA

A. J. Rosakis
Graduate Aeronautical Laboratories, California Institute of Technology, Pasadena, California, USA

Received 13 February 2001; revised 9 July 2001; accepted 14 July 2001; published 23 August 2002.

[1] A substantial effort has been devoted in the past toward modeling earthquake source mechanisms as dynamically extending shear cracks. Most of the attention was focused on the subsonic crack speed regime. Recently, a number of reports have appeared in the seismological literature citing evidence of intersonic rupture speeds during shallow crustal earthquakes. In the first part of this paper, we discuss direct experimental observations of intersonic in-plane shear crack growth along a weak plane joining two homogeneous, isotropic, linear elastic plates. Associated with the primary intersonic crack and at locations behind the propagating shear crack tip, a series of secondary tensile cracks, at a steep angle to the shear crack plane, were also observed. Motivated by these observations, subsonic and intersonic mode II crack propagation with a velocity weakening cohesive zone is analyzed in the main body of the paper. A cohesive law is assumed wherein the cohesive shear traction is either a constant or decreases linearly with the local slip rate, the rate of decrease governed by a slip rate weakening parameter. The cohesive shear traction is assumed to vanish when the crack tip sliding displacement reaches a characteristic breakdown slip. It is shown that a positive energy flux into the rupture front is possible in the entire intersonic regime. The influence of shear strength and of the weakening parameter on the crack propagation behavior is investigated. Crack tip stability issues are also addressed, and favorable speed regimes are identified. Estimates of the slip rate weakening parameter are obtained by using the theoretical model to predict the angle of the secondary cracks. The rest of the parameters are subsequently estimated by comparing the isochromatic fringe patterns (contours of maximum in-plane shear stress) predicted by the solution with those recorded experimentally. *INDEX TERMS:* 7209 Seismology: Earthquake dynamics and mechanics; 7260 Seismology: Theory and modeling; 8010 Structural Geology: Fractures and faults; *KEYWORDS:* intersonic, shear rupture, weak planes, fault mechanics

1. Introduction

[2] A majority of earthquakes are caused by sudden rupturing of the Earth's crust along a preexisting fault plane (weak plane in the Earth's crust) under the action of high ambient compressive and shear prestresses. The source process involves a sudden slip in some local region on the fault plane accompanied by a sudden stress drop over the slipping region. Elastodynamic shear crack models provide adequate approximations of the source mechanism and have been widely used, in conjunction with the radiated elastic wave field recorded by seismograms, to recover information about the rupture process [*Freund*, 1979; *Rice*, 1980; *Dmowska and Rice*, 1986; *Scholz*, 1990]. Average rupture speeds thus inferred for most shallow crustal earthquakes observed so far range from 0.7 to 0.9β, where β is the average speed of *S* waves (shear waves) in the surrounding rock body [*Heaton*, 1990; *Beeler and Tullis*, 1996]. Rupture propagation is very sensitive to the properties of the surrounding material and as such is a highly transient process. For average rupture speeds close to β, it is plausible that locally (on the portion of the rupture front where the slip is predominantly in-plane shear), for short durations, rupture speeds could be intersonic (speeds between β and the *P* wave speed or longitudinal wave speed, α). Indeed, evidence supporting such a scenario, at least over a portion of the faulting, has been reported in the literature [*Archuleta*, 1984; *Spudich and Cranswick*, 1984; *Olsen et al.*, 1997; *Hernandez et al.*, 1999; *Ellsworth and Celebi*, 1999; *Bouchon et al.*, 2000, 2001].

[3] However, up to now, there have been no direct laboratory observations of intersonic shear cracks. Indeed,

0148-0227/02/2001JB000460$09.00

propagating mode II cracks (either subsonic or intersonic) are not observed in homogeneous solids. Pre-existing cracks subjected to asymmetric loading curve or kink and tend to propagate in directions oblique to the initial crack direction, usually by choosing a path that would make them locally tensile (mode I) [*Cotterell and Rice*, 1980]. However, fault ruptures leading to earthquakes almost always extend as planar cracks. Possible reasons for the planar growth are that a preexisting fault plane provides a weakened path which is preferential for crack extension and that the confining pressure reduces the effect of tensile circumferential stresses near the crack tip which might otherwise lead to oblique crack growth. Fault planes which are relatively new (with regard to geological timescales) may be considered as weak planes separating rock bodies with approximately the same elastic and thermal properties. As such, laboratory experiments investigating high-speed dynamic shear crack propagation along a weak plane joining two identical homogeneous, isotropic, linear elastic solids may shed light on the possibility of intersonic rupture speeds.

[4] For remotely loaded mode I cracks in homogeneous, isotropic, linear elastic solids the theoretical upper limit on the propagation speed, v, is the Rayleigh wave speed (c_R) of the material [*Freund*, 1990; *Broberg*, 1999b]. The energy flux into the crack tip region vanishes at c_R, and at higher speeds, no analytical solution can be found with positive energy flux into the tip [*Broberg*, 1989]. Indeed, positive energy flux is required because crack growth involves material separation, which is an energy consuming process, and hence a necessary condition for propagation of a crack is that energy be supplied from the outer stress field to the crack tip region. For remotely loaded mode II cracks, which are forced to propagate in a prescribed straight-line path or fault plane, crack speeds below c_R (sub-Rayleigh) and those in the intersonic regime are both permissible from similar energetic considerations. The crack speed regime between c_R and β is, however, forbidden. As a result, such cracks may either be purely sub-Rayleigh or purely intersonic but may not transition between the two regimes with a continuous variation of crack speed. Hence the upper limit on the propagation speed (according to the classical interpretation) for a remotely loaded mode II crack is α [*Broberg*, 1996]. On the basis of the same consideration the upper limit on the propagation speed for remotely loaded mode III cracks is β. The requirement of positive energy flow to the crack edge region is inescapable. Only in cases where energy is supplied directly to the crack tip without recourse to elastic stress waves does crack propagation at any speed may become possible [*Winkler et al.*, 1970; *Curran et al.*, 1970].

[5] Experimental observations in the laboratory typically show realistic mode I crack speeds that are <60% of c_R [*Fineberg and Marder*, 1999]. In brittle solids, at $\sim$30–40% of c_R the microbranching instability sets in, whereby the crack follows a wavy path, producing increasingly rough fracture surfaces, and repeatedly attempts to branch [*Ramulu and Kobayashi*, 1985; *Ravichandar and Knauss*, 1984b; *Gao*, 1993]. Eventually, successful branching into multiple cracks occurs at speeds much below c_R, thus making the theoretical limit inaccessible. Also the height of the process region (e.g., zone of microcracking) increases substantially at high fracture speeds, indicating a strong increase in the fracture energy required to sustain propagation at these speeds [*Ravichandar and Knauss*, 1984a; *Johnson*, 1992]. W. G. Knauss and his coworkers have shown that if the height of the process region can be restrained to a thin layer along the crack path, thus suppressing branching, then crack speeds can approach the theoretical limiting speed, c_R [*Lee and Knauss*, 1989; *Washabaugh and Knauss*, 1994]. They observed mode I cracks along a weak plane between two identical brittle solids, asymptotically approaching the theoretical limit c_R as the cohesive strength of the plane was reduced. As mentioned before, propagating mode II cracks are usually not observed in homogeneous isotropic solids. Sustained mode II crack growth in such media is possible only if high compressive ambient stresses are acting on the body preventing crack opening [*Melin*, 1986; *Broberg*, 1987]. Directional stability of a mode II crack may also be sustained if it propagates along a weak layer. Earthquake fault ruptures may be approximated as dynamically growing shear (mixed mode II and mode III) cracks along preexisting weak fault planes in the presence of high ambient compressive and shear prestresses. The mode mix as well as rupture speed varies with position along the rupture front, and hence portions of the front where the deformation is predominantly mode II may attain intersonic speeds. Confirming the possibility, *Rosakis et al.* [1999, 2000], provided the first direct and unambiguous laboratory evidence of intersonic mode II cracks in the laboratory along weak planes in a brittle solid. The experimental observations are summarized in section 2.

[6] Hereinafter we concentrate exclusively on mode II cracks, and henceforth the term shear crack refers to one around which the deformation field exhibits mode II symmetries. In probably the first study on intersonic shear cracks, *Burridge* [1973] analyzed the problem of a mode II crack growing self-similarly from zero initial length along an interface between two identical half-spaces held together by Coulomb frictional contact and subjected to preimposed uniform normal and shear stresses. In effect, he considered the limiting case of zero cohesive energy together with a finite stress limit or, in other words, a propagating stress drop. He found that for subsonic crack speeds a positive peak in shear stress propagating along with the shear wave front appears ahead of the crack tip. This peak in shear stress is observed to increase in magnitude as the crack speed increases, and Burridge postulated that it might lead to a secondary slip zone in front of the main crack tip provided the limiting static friction is small. He argued that a shear crack on such an interface will propagate at c_R and, if the limiting static friction is small, it would propagate at α. He also noted that the crack tip stress singularity for intersonic mode II cracks is <1/2 and that it is a function of crack speed. *Andrews* [1976] numerically analyzed the problem of transient symmetric expansion of a mode II crack propagating along a prescribed path with a linearly slip-weakening cohesive zone [*Ida*, 1972; *Palmer and Rice*, 1973] under the action of a uniform remote shear stress. Corroborating Burridge's prediction, Andrews found that the expanding shear crack rapidly accelerates to speeds close to c_R and, if the limiting static friction is not high enough, it initiates a secondary slip zone in front of it, which coalesces with the main crack and that the combination was found to propagate at speeds around 1.5β. His

observation describes one possible mechanism for a subsonic shear crack to cross the forbidden speed regime between c_R and β. He pointed out that for intersonic cracks, where the crack tip stress singularity is <1/2, a nonzero fracture energy is supported only for the case where the stress drop is not abrupt; that is, the crack tip region must have a finite extent. *Das and Aki* [1977] analyzed transient mode II crack expansion in an infinite, isotropic, homogeneous, elastic solid under uniform remote shear stress using a boundary integral method. The crack tip was modeled as a structureless point, and dynamic friction was assumed to act on the crack faces. Using a critical stress criterion, they confirmed the numerical results of *Andrews* [1976].

[7] *Freund* [1979] obtained the asymptotic stress and particle velocity fields around a steady state intersonic mode II crack, constrained to propagate along a straight-line path. He showed that the stress field predicts two Mach waves radiating from the crack tip. Stresses are singular not only at the crack tip but all along the Mach fronts, with the same order of singularity as that at the tip. In addition, across the Mach front the normal stress and normal velocity perpendicular to the front are continuous, whereas the shear stress and tangential velocity suffer an infinite jump. Hence these fronts are shear Mach waves. He also commented upon the curious speed of $\sqrt{2}\,\beta$, at which an intersonic crack behaves "subsonic-like" and the two trailing Mach waves disappear. He investigated the problem of transient symmetric expansion of a mode II crack under remote shear stress which was studied numerically by *Andrews* [1976] and *Das and Aki* [1977]. Using a critical stress criterion, he concluded that the terminal speed for a subRayleigh mode II crack is c_R and that an intersonic mode II crack would begin to grow at a speed greater than $\sqrt{2}\,\beta$ and would quickly accelerate to α. *Burridge et al.* [1979] investigated the stability of a steady state mode II semi-infinite crack with a slip-weakening cohesive zone driven by a point load acting on the crack faces a finite distance from the tip. They solved the governing integral equation numerically and concluded that for a dynamic mode II crack the crack speed regimes $v < c_R$ and $\beta < v < \sqrt{2}\,\beta$ are inherently unstable, the speed regime $\sqrt{2}\,\beta < v < \alpha$ is stable, while the speed regime $c_R < v < \beta$ is forbidden. *Rice* [1980], *Das* [1985], and *Dmowska and Rice* [1986] summarized the literature on dynamic shear crack propagation and its application to modeling the earthquake source process.

[8] *Broberg* [1989] gave an elegant summary of the admissible crack speed regimes for mode I, mode II, and mode III cracks (all propagating along a predetermined straight-line path) on the basis of the requirement of a positive energy flux to the crack tip region. *Broberg* [1994, 1995] also solved analytically the problem of a self-similar intersonic mode II crack expanding symmetrically from zero initial length under the action of a remote uniform shear stress. He showed that the dynamic energy release rate depends on the extent of the process region as $(d/a)^{(1-2q)}$, where d is the extent of the process region, a is the crack length, and q is the speed dependent crack tip stress singularity. Except for $v = \sqrt{2}\,\beta$, where $q = 1/2$, a vanishing process region predicts a vanishing energy flux into the tip. He assumed a Barenblatt-type process region (more exactly a cohesive traction distribution that varies linearly with position) near the crack tip and computed the energy flux into the intersonic crack tip region. For the chosen process region type he showed that the requirement of constant fracture energy independent of crack speed would accelerate an intersonic crack all the way up to α. He also investigated the effect of transient crack acceleration on the near tip fields for a semi-infinite intersonic mode II crack [*Broberg*, 1999a]. *Johnson* [1990] showed that steady state unidirectional mode II crack growth is possible in earthquake events, provided that one of the leading edges associated with an initially extending rupture front encounters a barrier (region of high shear strength). In his finite element simulations he observed terminal speeds close to α. The case of rupture on a fault within a low wave speed zone sandwiched between two identical high wave speed materials was investigated numerically by *Harris and Day* [1997]. Depending on the width of this zone and the location of the fault within the zone, a host of rupture speeds were predicted ranging from below β all the way up to $\sqrt{2}\,\beta$ of the higher wave speed material but never exceeding it.

[9] Some of the recent analytical and numerical work on dynamic shear cracks was motivated by the experiments of A. J. Rosakis and his coworkers on intersonic crack propagation in homogeneous, isotropic solids [*Rosakis et al.*, 1999, 2000], in bimaterials [*Lambros and Rosakis*, 1995; *Singh et al.*, 1997; *Rosakis et al.*, 1998], and in transversely isotropic solids [*Coker and Rosakis*, 2001] all of which feature special directions of inhomogeneity in fracture toughness (i.e., planes of reduced fracture toughness). *Gao et al.* [1999] made an interesting comparison of intersonic cracks with intersonic glide edge dislocations and developed a unified treatment for investigating the existence of radiation-free intersonic speeds for either system. *Huang et al.* [1999] derived the asymptotic fields around an intersonically propagating mode II crack in a transversely isotropic material. They showed that a radiation-free intersonic speed exists for a mode II crack in a transversely isotropic solid, similar to $\sqrt{2}\,\beta$ for the homogeneous case, where the crack tip dynamic energy release rate is finite. *Yu and Suo* [2000] developed a unified method based on analytic function theory to obtain the near-tip fields for a quasi-static/subsonic/intersonic crack in a homogeneous solid or along a bimaterial interface with the constituents being either isotropic or anisotropic. They used a Dugdale-type cohesive zone model (constant cohesive traction) and identified those crack speed regimes that result in negative cohesive zone length being forbidden.

[10] *Needleman* [1999] performed a finite element simulation of the intersonic shear crack experiments of *Rosakis et al.* [1999] using a cohesive surface constitutive relation for the weak crack path. He found that a shear crack initiating from a precrack along the weak path either propagates at c_R or accelerates to a near constant intersonic speed above $\sqrt{2}\,\beta$. He examined the effect of shear strength of the interface, the fracture energy, and the duration of the loading pulse on the transition from a sub-Rayleigh to an intersonic speed, as well as on the terminal speed achieved. *Abraham and Gao* [2000] performed an atomistic simulation of shear crack propagation along a weak interface characterized by a Lennard-Jones potential, joining two harmonic crystals. Their simulations showed that a shear dominated crack, soon after initiation

accelerates to c_R and then nucleates an intersonic daughter crack that travels at α, in accordance with the predictions of *Burridge* [1973] and *Andrews* [1976]. When the applied strain was completely relaxed after the initiation of the daughter crack, they found shear crack propagation at $\sqrt{2}\,\beta$, similar to the behavior observed in the experiments of *Rosakis et al.* [1999]. Using a spectral boundary element scheme, *Geubelle and Kubair* [2001] numerically studied the problem of transient initiation and propagation of a mixed mode in-plane crack in its own plane under the action of remote uniform mixed mode loading. Using a quasi-linear cohesive failure model, they observed that a shear-dominated crack can attain intersonic speeds either by initiation of a secondary slip zone in front of the tip (the Burridge-Andrews mechanism) or simply by a rapid, but smooth acceleration through the forbidden regime. The latter case, which was also observed by *Johnson* [1990], is in contradiction with the theoretical prediction that an in-plane crack with a continuously varying speed cannot accelerate through c_R. During steady state intersonic crack growth it was found that the cohesive failure occurred entirely in shear even under far-field mixed mode loading, consistent with analytical predictions. *Gao et al.* [2001] studied the transition of a subsonic mode II crack to intersonic speeds using a cohesive fracture criterion and showed that the predictions of continuum elasticity theories are captured very well by atomistic simulations.

[11] In the geophysics literature, more emphasis has been placed on the analysis of symmetrical expansion of two- and three-dimensional (2-D and 3-D) shear cracks of finite size rather than on semi-infinite mode II or mode III cracks. The reason for this emphasis seems to be due to the fact that actual faults have finite dimensions, and if primary interest is on the details of seismic radiation due to fault motion, then these fault dimensions must be included. On the other hand, if primary interest is on the fracture process, then the actual fault dimensions are of lesser importance, and semi-infinite crack models appear to be suitable. Our current work is primarily motivated by the experimental observations of intersonic shear cracks in our laboratory and is pursued with an aim toward providing a satisfactory analytical model to explain the various features of the rupture process. Therefore a semi-infinite cohesive shear crack model was chosen and examined critically for its ability to explain the various features observed during intersonic shear rupture. In section 2 a brief description is provided of the experimental procedure, and evidence of intersonic shear cracks is presented. The experimental observations are compared with the singular solution of *Freund* [1979], thus motivating the necessity of a cohesive zone model. In sections 3, 4, and 5 a velocity weakening cohesive zone model for steady state dynamic mode II crack propagation is proposed and analyzed. The cohesive shear traction is assumed to decrease linearly with increasing local slip rate. The governing equations are solved using a standard technique in analytic function theory and the nature of the predicted near-tip fields is examined. In section 7 a propagation criterion is imposed, which requires a constant breakdown slip at the physical crack tip (rear end of the cohesive zone), and its predictions on the fracture energy dissipated, critical cohesive zone length, and stability of crack growth are discussed. In sections 6 and 8 the ability of the model to predict the various features observed during intersonic mode II crack propagation is examined, and the parameters of the model are extracted. Finally, in section 9 the possibility of self-healing slip pulses in our laboratory specimens is briefly discussed.

2. Experimental Observations of Intersonic Shear Cracks

[12] Experiments were performed in the laboratory to verify the possibility of intersonic mode II rupture speeds along a weak plane in an otherwise constitutively homogeneous, isotropic, linear elastic solid. The experimental setup is shown in the inset of 1, along with the details of specimen geometry and the loading device. The laboratory specimens were made by bonding two identical plates (150 mm $\times$ 125 mm) of Homalite-100, a brittle polyester resin, as shown in the inset of 1. The thickness of the plates was either 4.8, 6.4, or 9.5 mm. Homalite-100 exhibits the property of stress-induced birefringence, enabling the use of dynamic photoelasticity for visualizing the stress state in the specimen. The bonding process was chosen carefully so that the constitutive properties of the bond are close to those of the bulk material. A polyester resin solution (99.5% by weight) was used for bonding, with methyl ethyl ketone peroxide as hardener (0.4%) and cobalt octate (0.1%) as catalyst. The bond was cured for 48 hours at room temperature. The thickness of the bond so obtained was $\sim$20–30 μm. A notch, 25 mm long and 2 mm wide, was machined on the upper half of the specimen along the bond line (see Figure 1). The relevant material properties of Homalite at high strain rates (of the order 10^3 s^{-1}) are shear modulus, μ = 1.9 GPa; Poisson's ratio, ν = 0.34; c_R (plane stress) = 1155 m/s; β = 1255 m s^{-1}; and α (plane stress) = 2187 m s^{-1}. The tensile strength σ_u of bulk Homalite is $\sim$35 MPa and the shear strength of the bond τ_o, as measured using a conventional Iosipescu shear test fixture is around 12–16 MPa. Thus we constructed a material system which, although not monolithic, can be considered homogeneous with regard to its linear elastic constitutive description. However, the strength and fracture toughness along the bond line are lower, so that the material is inhomogeneous with regard to its fracture properties.

[13] A schematic illustration of the experimental setup is shown in 1. Dynamic photoelasticity was chosen for recording the stress field near the propagating crack tip because of its ability to visualize shear Mach waves, anticipated by the intersonic crack solutions. The specimen was subjected to asymmetric impact loading with a cylindrical projectile fired from a high-speed gas gun. The projectile was 75 mm long and 50 mm in diameter and was made of hardened steel. Compressed air at 83 kPa to 0.6 MPa was used as the driving medium, which resulted in projectile velocities ranging from 8 to 40 m s^{-1}. A steel buffer was bonded to the specimen at the impact site to induce a planar loading wave front. The compressive longitudinal wave diffracts around the notch loading it, initially, in a predominantly shearing mode [*Lee and Freund*, 1990]. The loading pulse is of the ramp type, with a risetime of 27 μs and a peak compressive stress of 54 MPa. The risetime corresponds roughly to the time taken for a longitudinal wave to traverse twice the length

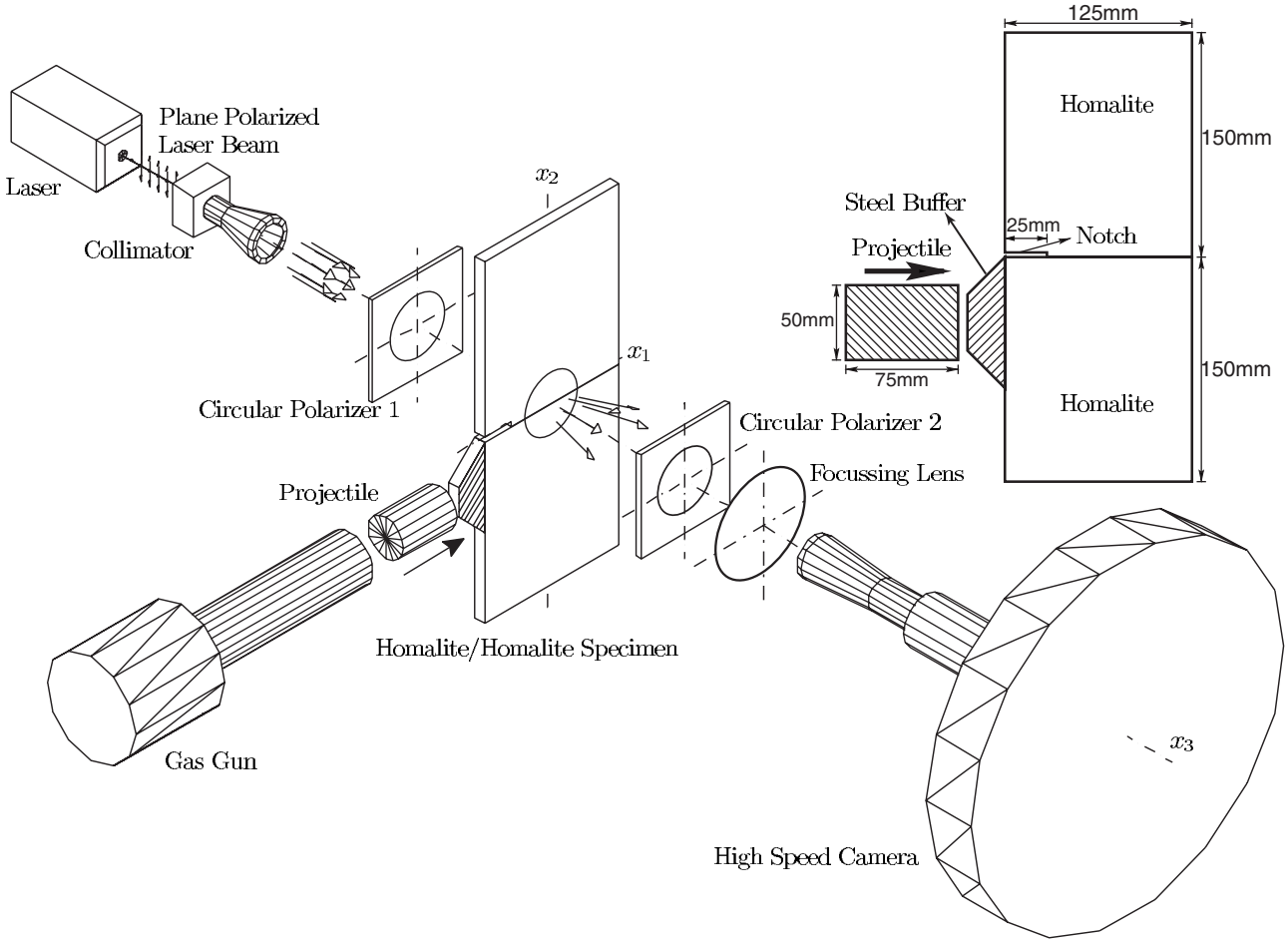

Figure 1. Dynamic photoelasticity setup showing a Homalite/Homalite specimen placed inside a circular polariscope and being subjected to impact shear loading by a projectile fired from a high-speed gas gun. The resulting isochromatic fringe patterns are recorded by high-speed photography. The specimen geometry is shown in the inset.

of the projectile, which is also the time for which the projectile is in contact with the steel buffer. A notch was preferred to be the crack initiation site instead of a mathematically sharp precrack to prevent the transmission of stress waves into the top half and also to increase the toughness initiation threshold. The dynamic stress field produced by the impact loading was recorded using photoelasticity in conjunction with high-speed photography. A coherent, monochromatic, plane-polarized, collimated laser beam of 50 mm diameter was transmitted through the specimen. An argon ion pulsed laser was used as the light source, operating at a wavelength of 514.5 nm (green). The specimen was placed in a light field circular polariscope resulting in an isochromatic fringe pattern due to stress induced birefringence in Homalite. Photoelasticity is a common optical technique used in solid mechanics applications which provides real-time full field information about the stress state, and the reader is referred to *Dally and Riley* [1991] for further details. The isochromatic fringe pattern is recorded by a rotating mirror type high-speed camera capable of recording 80 frames at framing rates up to 2 million frames per second. The generation of the isochromatic fringe patterns, which are contours of constant maximum in-plane shear stress (τ_{max}) is governed by the stress optic law

$$\sigma_1 - \sigma_2 = 2\tau_{max} = \frac{nF_\sigma}{h}, \tag{1}$$

where F_σ is the material fringe constant, h is the specimen thickness, σ_1, σ_2 are the two principal stresses in the plane, and n is the isochromatic fringe order. For Homalite-100, F_σ = 22.6 kN m^{-1}.

[14] Figure 2 shows a selected sequence of isochromatic fringe patterns around a shear crack initiating from a notch and propagating along the weak plane joining two Homalite plates. The time elapsed after impact as well as the crack tip speed (after initiation) is shown in each frame. The sequence is drawn from two nominally identical experiments differing only in the position of the field of view. Speed of the projectile at the time of impact was $\approx$27 m s^{-1}. In the first three frames (Figures 2a–2c) the field of view of 50 mm diameter is centered on the weak plane, 20.6 mm ahead of the notch tip. In Figure 2a we can see the stress waves from the impact site diffracting around the notch tip and simultaneously observe the stress concentration build-

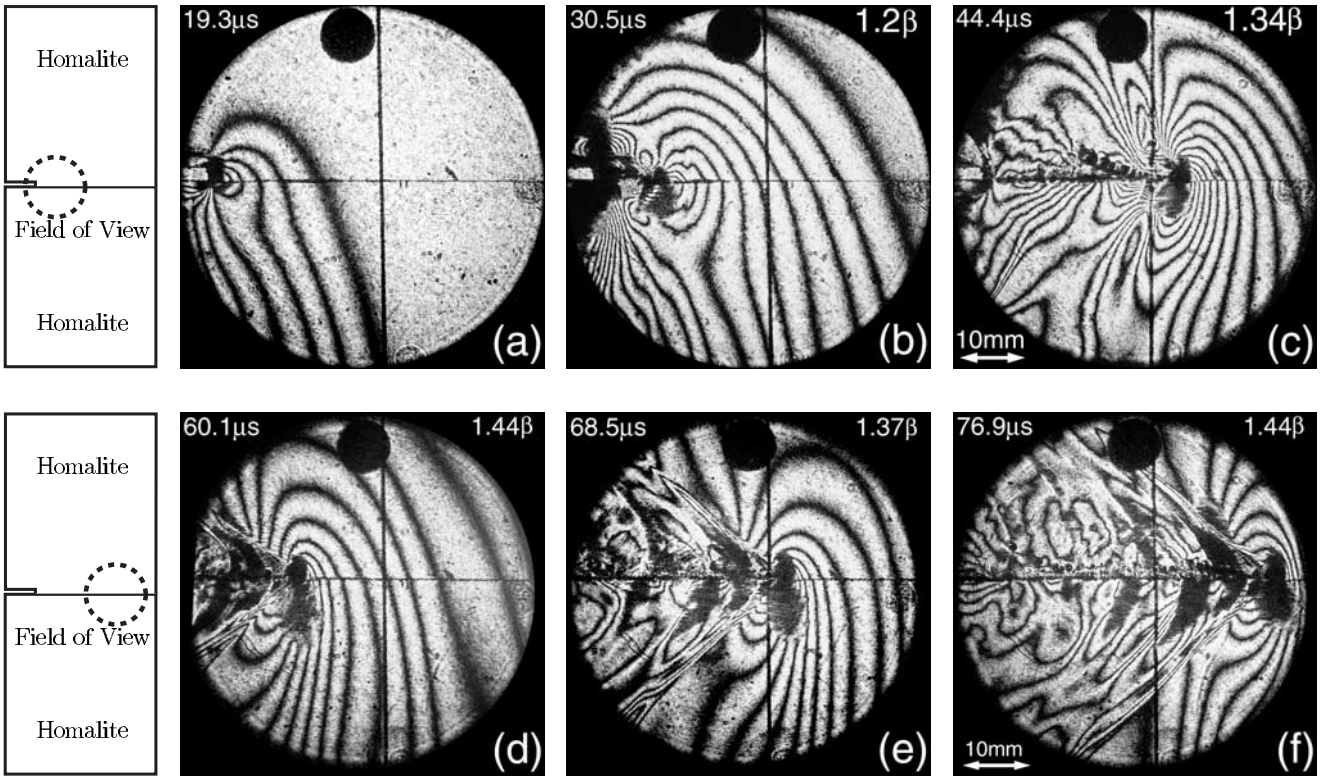

Figure 2. Isochromatic fringe pattern around a crack initiating from a single edge notch and propagating along a weak plane in Homalite. Impact speed ≈27 m s^{-1}. (a–c) Field of view of 50 mm diameter centered 20.6 mm ahead of the notch tip. (d–f) Field of view of 50 mm diameter centered 63.1 mm ahead of the notch tip. The two Mach waves radiating from the intersonic crack tip can be clearly distinguished.

ing up. In Figure 2b a shear crack has just initiated from the notch tip and begins to propagate along the weak plane. The nature of stress wave loading acting on the propagating crack would cause the crack faces to move toward each other, if possible [*Lee and Freund*, 1990]. However, the crack faces in their rest configuration are already in contact (but traction free) and so are constrained against such a movement. This results in a negligible negative mode I component at the tip, and the propagating crack may be considered to be a pure mode II crack, albeit with negative normal tractions acting on the crack faces (which annul the negative mode I stress intensity factor required at the tip due to the mode mix of far-field loading). Also, note that the crack speed is already intersonic at this stage, confirming the analytical predictions of *Andrews* [1976], *Freund* [1979], *Broberg* [1989], etc., that intersonic mode II crack growth is energetically permissible. Figure 2c shows an increased stress intensity around the propagating crack tip and in addition we can discern a series of shadow spots all lined up at a steep angle to the crack plane behind the crack tip. In Figures 2d–2f the field of view of 50 mm diameter is centered 63.1 mm ahead of the notch tip. In Figure 2d we see a crack entering the field of view around which the shape of the isochromatic fringe pattern has changed dramatically. In Figures 2e and 2f we can clearly distinguish two lines radiating from the crack tip across which the fringe pattern changes abruptly (lines of stress field discontinuity). These two lines correspond to the two traveling shear Mach waves, which limit the spread of shear waves emanating from the crack tip as it propagates along the interface at intersonic speeds. The angle, ξ, the Mach waves make with the crack faces is related to the crack speed through

$$\xi = \sin^{-1}(\beta/v). \tag{2}$$

The crack speed and the Mach angle in Figures 2e and 2f are in close proximity, and the nature of the isochromatic fringe pattern is very similar, indicating that the propagating crack at this stage may be approximated to have reached a steady state.

[15] Typical crack tip speed histories for two identical experiments varying only in the position of the field of view are shown in Figure 3. Crack tip speeds were determined using two methods. In the first method a second-order interpolating polynomial is obtained for every three successive points in the crack length history, which is then differentiated with time to give the crack speed for the midpoint. In the second method, crack tip speeds for frames in which the Mach waves can be clearly distinguished are obtained by measuring their angle of inclination to the crack faces and using equation (2). The variation of the crack tip speed with crack length obtained using the first method is shown in Figure 3a, whereas that obtained by the second method is shown in Figure 3b. Crack length includes length of the initial notch, which was ~25 mm. From Figure 3a we see

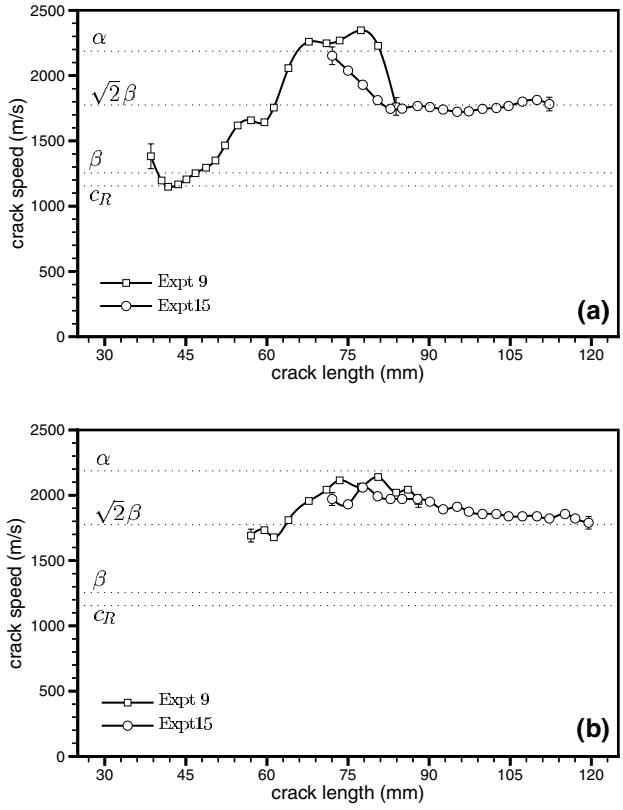

Figure 3. Evolution of crack speed as the crack propagates along the weak plane. Experiment 9 corresponds to an impact speed of 26.8 m s^{-1}, and the field of view of 50 mm was centered at 29.1 mm ahead of the notch tip. Experiment 15 corresponds to an impact speed of 27.7 m s^{-1}, and the field of view of 50 mm was centered at 63.1 mm ahead of the notch tip. (a) Crack speed obtained from crack length history. (b) Crack speed obtained from Mach angle measurements.

that the initially recorded crack tip speed is close to the shear wave speed of Homalite (within experimental error of ±100 m s^{-1}) beyond which it accelerates (at the order of 10^8 m s^{-2}), thus becoming intersonic. Thereafter, it continues to accelerate up to the plane stress longitudinal wave speed of Homalite, following which it decelerates and ultimately reaches a steady state value of about $\sqrt{2}$ times the shear wave speed. As seen in Figure 2, the Mach wave angle under steady state conditions reaches an almost constant value around 43°–45°, corresponding to a crack tip speed slightly higher than $\sqrt{2}\ \beta$. For the recent Izmit (Turkey) earthquake, *Bouchon et al.* [2000, 2001] reported that the portion of rupture zone propagating toward the east attained a remarkably high average speed of 4.7 km s^{-1}. With the average shear wave speed in crustal rocks at those depths being around 3.4–3.5 km s^{-1}, the rupture speed was $\sim 1.4\beta$. This is very close to $\sqrt{2}\ \beta$, the speed around which a steady state intersonic shear crack was observed to propagate in our experiments. Note that the crack tip speed estimate from the Mach wave angle (whenever these are easily discernible) is more accurate compared to that obtained from the crack length history due to the inherent propagation of errors in the differentiation process. It should be recalled here that the speed regime between c_R and β is forbidden by theory based on energy considerations. Hence a crack will have to jump discontinuously from the sub-Rayleigh regime to the intersonic regime. However, another possibility for generating such intersonic speeds is to bypass this forbidden regime by nucleating a crack in front of the initial notch that instantaneously starts to propagate at a speed above β. Within our experimental time resolution the second scenario seems to be the most probable.

[16] Figure 4b shows a postmortem photograph of a portion near the notch tip on the upper half of the test specimen. Figure 4a shows an illustration of the specimen with the area photographed shown as a dashed rectangle. Starting from a finite distance ahead of the notch tip along the crack path, a series of short opening cracks, parallel to each other and steeply inclined to the main shear crack path, can be observed. These secondary cracks were observed all along the main crack path on the upper half, but no such cracks were observed in the lower half of the specimen. It can be concluded that these cracks have initiated on the upper crack face, propagated a finite distance (varying from a few microns to a few millimeters) slightly off-vertical into the upper half of the specimen and subsequently got arrested. Occasionally, a few cracks have gone farther. The broken specimens are carefully reassembled, and the angle of inclination of the secondary cracks to the vertical (line perpendicular to the crack plane) was measured. The measurements were made on specimens from five different experiments and Figure 4c shows a variation of the secondary crack angle with frequency (number of secondary cracks inclined at the same angle). It was found that the angle of inclination varies roughly from 8° to 13°, with an average of about 10.6°. Within the measurement error of ±1°, no strong correlation was found between the secondary crack angle and the main shear crack speed. The angle of inclination was found to reduce slightly toward the edge of the specimen, possibly due to the influence of the free boundary. Cracks that grew longer curved toward the vertical, but the initial orientation of all of them was almost the same. Most of the secondary cracks, especially the short ones seem to have a 3-D structure, in that they did not extend through the specimen thickness.

[17] The initiation, propagation, and arrest of these cracks can be observed in real time. The high-speed images of the isochromatic fringe pattern around the main shear crack tip contain information about the initiation and the growth of these cracks. A typical photograph in which the phenomenon can be clearly distinguished is shown in Figure 5a. A series of symmetric shadow spots, associated with the strong deformation around the secondary mode I crack tips, originate on the shear crack face, propagate a finite distance into the upper half of the specimen, and subsequently arrest. Such a series of shadow spots surrounding these secondary cracks are also clearly distinguishable in Figure 2c. The centers of all these shadow spots fall on almost a straight line inclined at ~23° (α*) to the crack face. From this measure, as well as the small inclination of these cracks from the vertical ($\theta^* \approx 11°$) and from the speed of the main shear crack, an estimate of their propagation speed is obtained to be $\sim 0.6\beta$. The symmetric nature of the shadow spots reveals the tensile (mode I) nature of these secondary cracks. If we extend the line passing through the center of

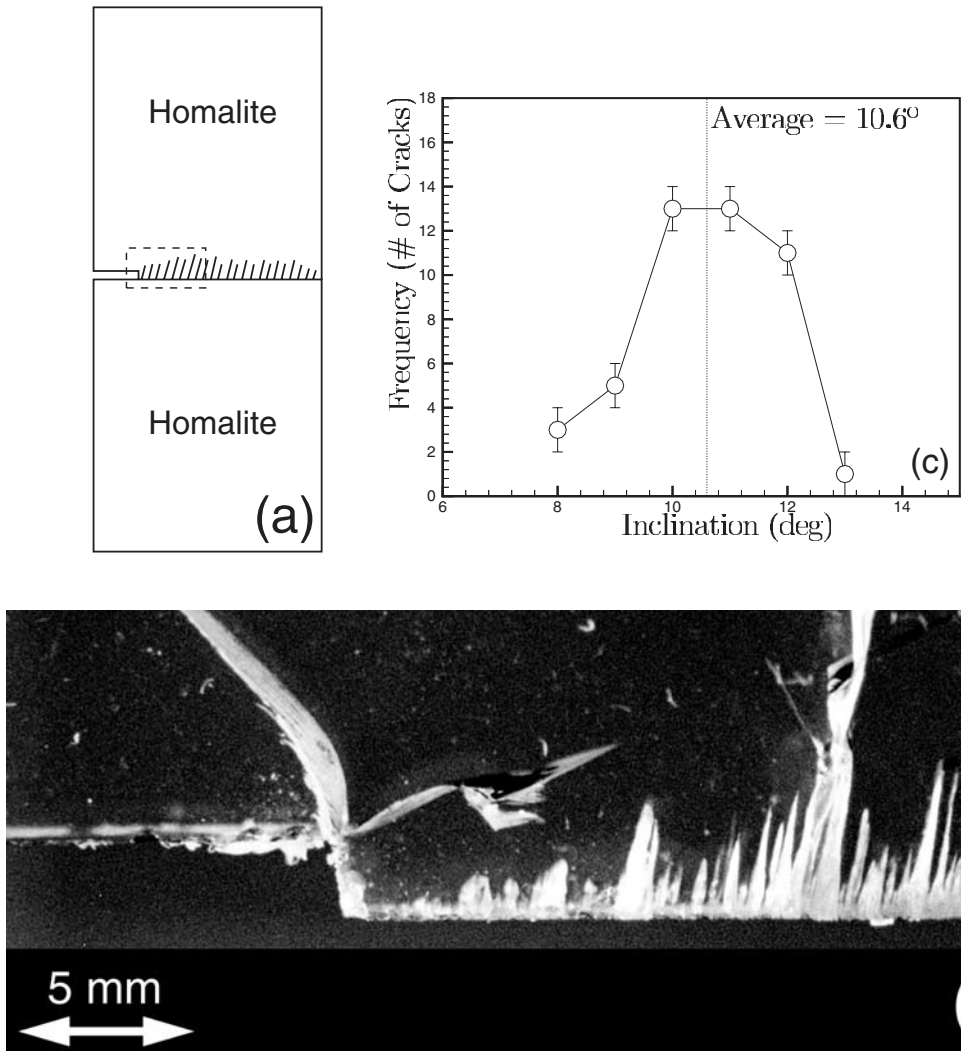

Figure 4. Secondary cracks formed on the tensile half of the specimen during intersonic shear crack growth. (a) Illustration of the specimen showing the location and orientation of the secondary tensile cracks (not to scale). (b) Magnified photograph of the region delineated by the dashed rectangle in the illustration in Figure 4a. (c) Measured data on the inclination of the secondary cracks to the vertical.

the shadow spots to the crack face, we can readily see that they originate a finite, albeit a small, distance behind the main crack tip. Hence formation of these secondary cracks is not akin to the typical branching phenomenon observed in high-speed subsonic crack propagation. Nor are they akin to the echelon cracks formed in front of a shear crack when its kinking into a tensile crack is prevented due to overall compressive stresses. These secondary, subsonic, opening mode cracks behind the main intersonic shear crack tip cannot be explained completely based on the asymptotic solution for a traction free intersonic crack. The stress component σ_{11} (direct stress parallel to the crack faces) around the intersonic shear crack tip is tensile in the top half of the specimen, whereas it is compressive in the bottom half. This explains why the opening cracks are observed only in the tensile half of the specimen. If the cracks originated on a traction-free surface, then we would expect them to propagate vertically (perpendicular to the crack plane). The inclination of the secondary cracks from the vertical can only be explained in terms of a more complex state of stress at the initiation site. As mentioned before, it is likely that the crack faces are in contact and subsequently undergo frictional sliding, resulting in a biaxial state of stress at the initiation site. However, most of these cracks seem to originate only a couple of millimeters behind the main crack tip, and in the absence of overall normal compression, a simple way to include the frictional stress at the initiation site is to introduce a shear cohesive zone of finite size behind the tip. Indeed, subsequently, we introduce a velocity weakening line cohesive zone at the intersonic crack tip to explain the inclination of these secondary cracks to the vertical. Figure 5b shows an illustration of the region near the crack tip that explains our interpretation as to the origin and directivity of the secondary tensile cracks. The main intersonic shear crack is propagating with a line cohesive zone of length L in front of it. The secondary cracks originate on the top cohesive surface, where the stress state is 2-D, with a tensile direct stress σ parallel to the interface along with a local shear cohesive traction, $-\tau$. With the biaxial state of stress at the

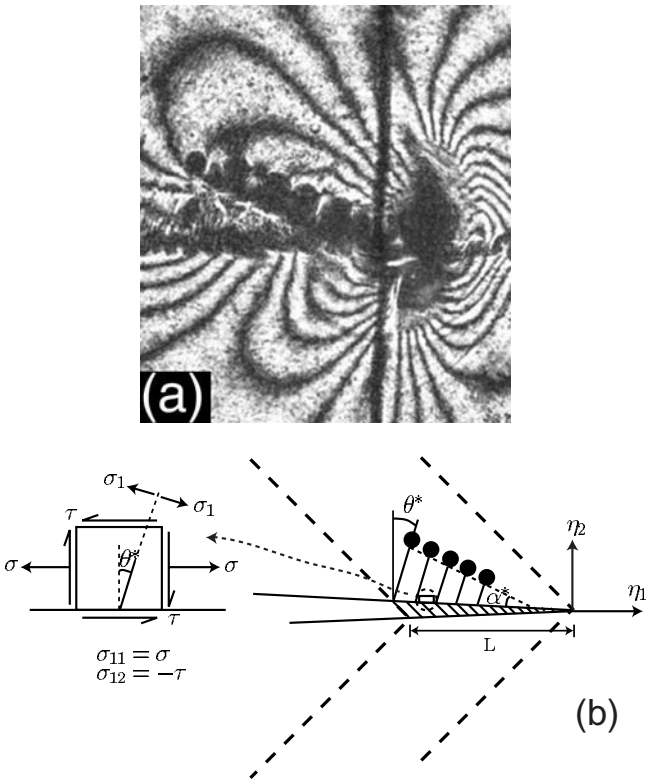

Figure 5. Formation of secondary tensile cracks during intersonic shear crack growth along a weak plane in Homalite. (a) Isochromatic fringe pattern showing the initiation and propagation of secondary cracks behind the main intersonic crack. (b) An illustration of the stress state on the crack face, providing an explanation for the inclination of these secondary cracks to the vertical.

initiation site the maximum principal tensile stress acts on a plane inclined at an angle θ* to the vertical, thus explaining the off-vertical orientation of these cracks. The driving force leading to the initiation and growth of these secondary cracks is provided by the near-tip field associated with the main intersonic shear crack. As the intersonic shear crack moves farther away from the initiation site of the secondary crack, the driving force acting on it falls, leading to its eventual arrest.

[18] Another motivation to study intersonic shear cracks with a finite sized shear cohesive zone is shown in Figure 6. It shows a sequence of isochromatic fringe patterns around an intersonic mode II crack along a weak plane in Homalite-100. Here the impact speed was 20.8 m s^{-1}, and the field of view of 50 mm diameter was centered on the weak plane, 38.2 mm ahead of the notch tip. Compared to the sequence shown in Figure 2, the impact speed here is lower, and also the field of view is much closer to the initiation site. In such a case, we see that the Mach waves radiating from the tip are not very sharp and have structure with a finite width. The finite width of the Mach waves is not modeled by the singular solution [*Freund*, 1979], which predicts mathematically sharp line Mach waves. An intersonic mode II crack model incorporating a cohesive zone of finite extent is required to model the structure of the Mach waves as well as the crack tip process zone.

[19] For intersonic mode II cracks the idealization of the crack tip process zone to a point-size dissipative region results in a physically unrealistic situation, wherein the requirement of a positive energy flux to the crack tip region is met only at $\sqrt{2}\ \beta$. On the contrary, the experimental observations show crack growth at all intersonic speeds. Moreover, the sharp crack solution predicts singular stresses at the crack tip as well as along the Mach waves with the same order of singularity as at the crack tip. However, such a singular stress distribution along propagating lines of stress discontinuity is clearly an idealization as the maximum stress at any point must be limited by the intrinsic strength of the material. A comparatively simple way to eliminate this difficulty would be to incorporate a cohesive zone of finite size in front of the tip [*Andrews*, 1976; *Broberg*, 1989]. In such a case, positive energy flux to the dissipative zone results at all intersonic speeds except at β and α. With such a model the finite strength of the interface can also be taken into account. In the subsequent sections, steady state subsonic and intersonic mode II crack propagation (along a weak interface) with a velocity weakening cohesive zone is analyzed. A line cohesive zone is introduced in front of the crack tip, with the traction on the cohesive surface decreasing linearly with increase in the local slip rate. Such a line cohesive zone has a natural motivation from the experiments described above, where the fracture process zone was mostly confined to a thin weak layer (the bond line) in front of the crack tip. Data on the dependence of cohesive shear traction on slip rate at the rates experienced in the experiments are unavailable. However, we assume that the dependence is linear, and we determine its slope by comparing the model predictions with the experimental observations.

3. A Cohesive Zone Model for Subsonic and Intersonic Mode II Rupture

[20] Consider a semi-infinite mode II crack with a line cohesive zone of length L in front of the tip, propagating at a constant speed v through a homogeneous, isotropic, linear elastic solid under 2-D plane strain or plane stress conditions (see Figure 7a). If the crack speed v during propagation, changes sufficiently smoothly, then the near-tip stress field at any instant is dominated by the instantaneous steady state solution [*Freund*, 1990]. The crack is constrained to propagate in its own plane and the crack speed can be either subsonic or intersonic ($0 < v < \alpha$). For planar deformation the displacement field u_α with respect to a fixed coordinate system (x_1, x_2) can be expressed in terms of two displacement potentials $\phi(x_1, x_2, t)$ and $\psi(x_1, x_2, t)$ as

$$u_\alpha(x_1, x_2, t) = \phi_{,\alpha}(x_1, x_2, t) + \epsilon_{\alpha\beta}\psi_{,\beta}(x_1, x_2, t), \qquad (3)$$

where $\epsilon_{\alpha\beta}$ is the 2-D alternator with $\epsilon_{11} = \epsilon_{22} = 0$ and $\epsilon_{12} = -\epsilon_{21} = 1$. The usual Cartesian index notation is employed, wherein repeated indices imply summation. Greek indices take the values 1 and 2 and roman indices take the values 1, 2, and 3. Also $(),\alpha = \partial(,)/\partial x_\alpha$ and an overdot on any field quantity represents derivative with respect to time.

[21] The strain field and stress field components can be expressed in terms of these displacement potentials using the strain-displacement relations and the generalized Hooke's

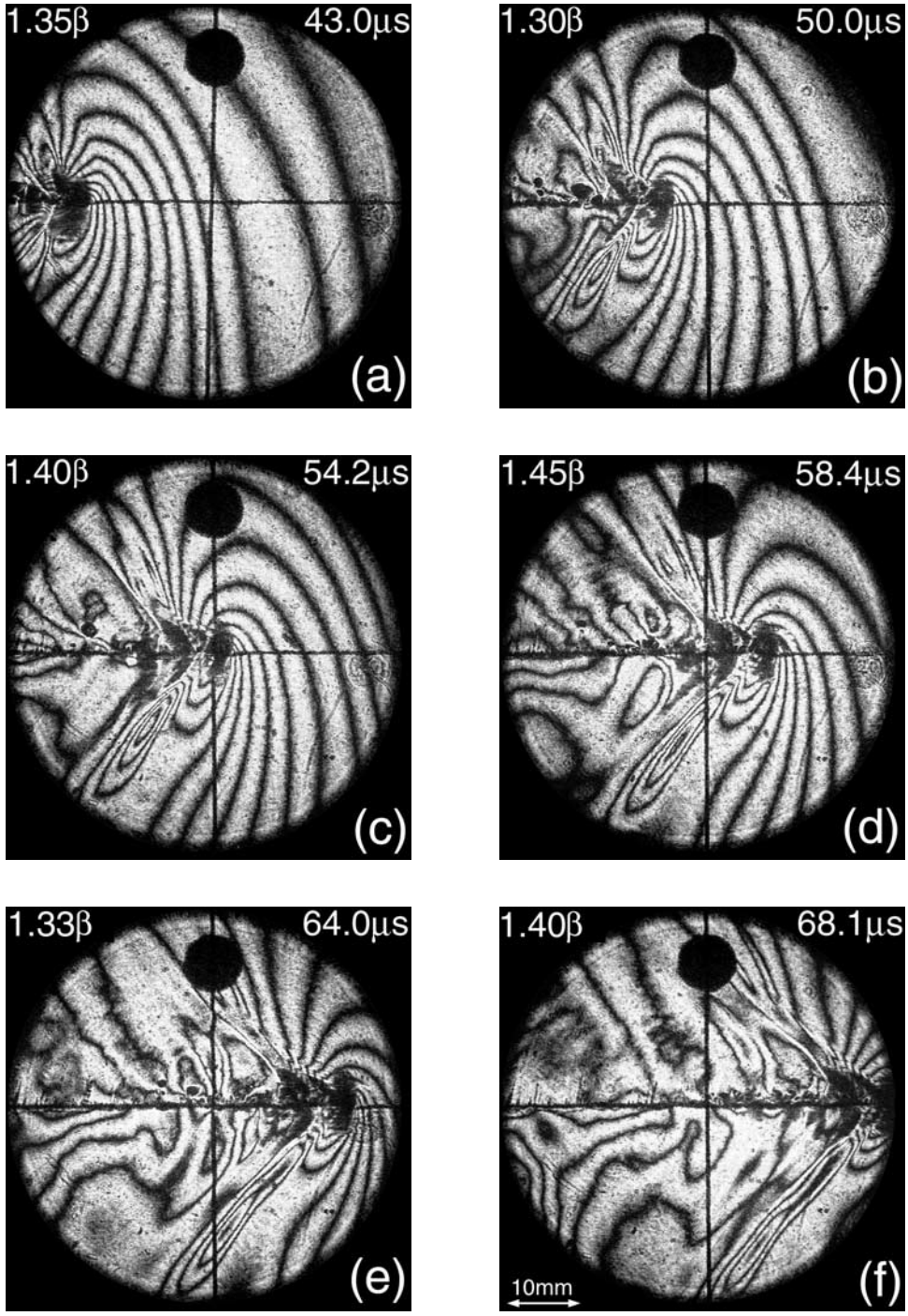

Figure 6. Isochromatic fringe pattern around a propagating intersonic crack along a weak plane in Homalite showing a cohesive zone of finite extent near the tip. Impact speed is 20.8 m s^{-1}. Field of view of 50 mm diameter was centered 38.2 mm ahead of the notch tip.

law. By introducing a moving coordinate system $(\eta_1, \eta_2) = (x_1 - vt, x_2)$ centered at the front end of the cohesive zone (see Figure 7a) and assuming that crack growth is steady state, one finds that the equations of motion in terms of ϕ and ψ reduce to [*Freund*, 1990; *Broberg*, 1999b]

$$\phi_{,11}(\eta_1, \eta_2) + \frac{1}{\alpha_l^2}\phi_{,22}(\eta_1, \eta_2) = 0 \qquad 0 < v < \alpha, \quad (4a)$$

$$\psi_{,11}(\eta_1, \eta_2) + \frac{1}{\alpha_s^2}\psi_{,22}(\eta_1, \eta_2) = 0 \qquad 0 < v < \beta, \quad (4b)$$

$$\psi_{,11}(\eta_1, \eta_2) - \frac{1}{\hat{\alpha}_s^2}\psi_{,22}(\eta_1, \eta_2) = 0 \qquad \beta < v < \alpha, \quad (4c)$$

where

$$\alpha_l = \sqrt{1 - \tfrac{v^2}{\alpha^2}}, \alpha_s = \sqrt{1 - \tfrac{v^2}{\beta^2}} \qquad \hat{\alpha}_s = \sqrt{\tfrac{v^2}{\beta^2} - 1}. \quad (5)$$

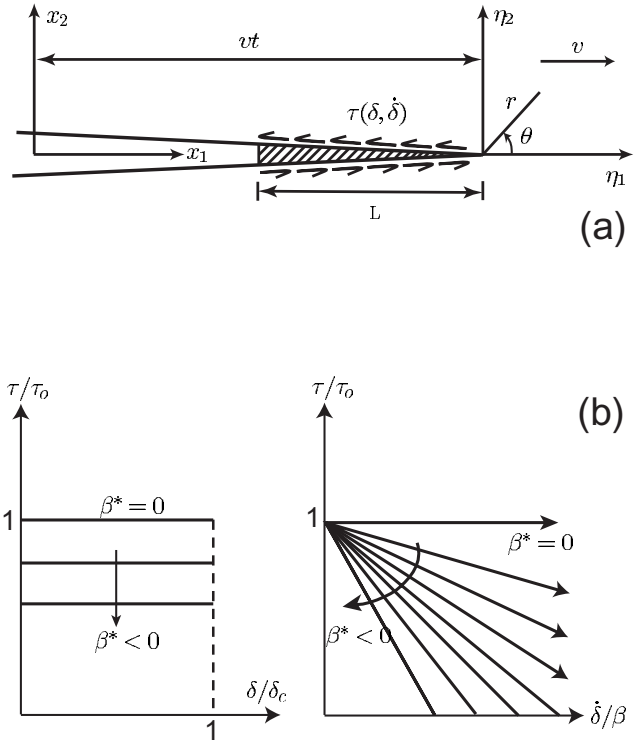

Figure 7. Dynamic in-plane shear crack in a homogeneous, isotropic, linear elastic solid with a velocity weakening cohesive zone. (a) Illustration showing the cohesive zone and the crack tip coordinate system. (b) Velocity weakening cohesive law relating the shear traction to the local slip and slip rate.

Thus the motion is governed by two elliptic equations in the subsonic case, whereas for the intersonic case it is governed by an elliptic and a hyperbolic equation.

3.1. Subsonic Case, $0 \le v < \beta$

[22] The most general solutions for the displacement potentials are [*Freund*, 1990]

$$\phi(\eta_1,\eta_2) = \mathrm{Re}\{F(z_l)\}, \tag{6a}$$

$$\psi(\eta_1,\eta_2) = \mathrm{Im}\{G(z_s)\}, \tag{6b}$$

where $F(\ )$ is a function, analytic with respect to its argument, $z_l = \eta_1 + i\,\alpha_l\eta_2$ everywhere in the z_l plane except on the crack faces and $G(\ )$ is a function, analytic with respect to its argument, $z_s = \eta_1 + i\alpha_s\eta_2$ everywhere in the z_s plane except on the crack faces. The stress and displacement fields may now be expressed in terms of the unknown functions F and G.

[23] For a mode II crack the displacement component u_1 is antisymmetric with respect to the crack plane, where as the component u_2 is symmetric with respect to the crack plane. Hence

$$F'^{-}(\eta_1) = -\bar{F}'^{-}(\eta_1), \tag{7a}$$

$$G'^{-}(\eta_1) = -\bar{G}'^{-}(\eta_1). \tag{7b}$$

The superscripts "+" and "−" stand for the limits $\eta_2 \to 0^+$ and $\eta_2 \to 0^-$, respectively. The traction boundary conditions on the cohesive surfaces and the crack faces are given by

$$\sigma_{22}^{\pm}(\eta_1) = 0 \qquad \eta_1 < 0, \tag{8a}$$

$$\sigma_{12}^{\pm}(\eta_1) = \begin{cases} \tau(\eta_1/L) & -L < \eta_1 < 0, \\ 0 & \eta_1 < -L, \end{cases} \tag{8b}$$

where $\tau(\eta_1/L)$ is the unknown cohesive traction distribution on the cohesive surfaces. Substituting for the stress fields in terms of F and G and incorporating the mode II symmetries from equation (7), we have

$$\begin{aligned}&\left(1+\alpha_s^2\right)\{F''^{+}(\eta_1) - F''^{-}(\eta_1)\} \\ &\quad +2\alpha_s\{G''^{+}(\eta_1) - G''^{-}(\eta_1)\} = 0 \qquad \eta_1 < 0,\end{aligned} \tag{9a}$$

$$\begin{aligned}&i\mu\Big[\alpha_l\{F''^{+}(\eta_1) + F''^{-}(\eta_1)\} + \frac{\left(1+\alpha_s^2\right)}{2} \\ &\quad \cdot\{G''^{+}(\eta_1) + G''^{-}(\eta_1)\}\Big] = \begin{cases} \tau(\eta_1) & -L < \eta_1 < 0, \\ 0 & \eta_1 < -L. \end{cases}\end{aligned} \tag{9b}$$

Equation (9a) implies that the function,

$$P(z) = \left(1+\alpha_s^2\right)F''(z) + 2\alpha_s G''(z), \tag{10}$$

which is analytic everywhere in the $z = \eta_1 + i\eta_2$ plane, except possibly along the crack line, is continuous across the crack line and it does not have any poles there. Hence $P(z)$ is an entire function. Furthermore, the vanishing of stress at remote points implies that $P(z) \to 0$ as $|z| \to \infty$. Hence $P(z)$ is a bounded entire function and by Liouville's theorem $P(z)$ is a constant. In particular, $P(z) = 0$ everywhere. Hence

$$G''(z) = \frac{-\left(1+\alpha_s^2\right)}{2\alpha_s}F''(z). \tag{11}$$

Equation (9b) becomes

$$iF''^{+}(\eta_1) - (-i)F''^{-}(\eta_1) = \begin{cases} \frac{4\alpha_s}{\mu R(v)}\tau(\eta_1/L) & -L < \eta_1 < 0, \\ 0 & \eta_1 < -L, \end{cases} \tag{12}$$

where $R(v) = 4\alpha_l\alpha_s - (1+\alpha_s{}^2)^2$ is the Rayleigh function. This is an inhomogeneous Hilbert problem. The general solution of equation (12) is given by *Muskhelishvili* [1963] and *Gakhov* [1990] and considering only the singular terms,

$$F''(z) = \frac{A_o}{\sqrt{z}} + \frac{1}{2\pi i}\frac{4\alpha_s}{\mu R(v)}\frac{1}{\sqrt{z}}\int_{-L}^{0}\frac{\sqrt{|\xi|}\tau(\xi/L)}{\xi - z}d\xi. \tag{13}$$

Following equation (7) we can readily conclude that A_o is pure imaginary.

[24] The shear stress ahead of the crack tip is given by

$$\begin{aligned}\sigma_{12}(\eta_1>0,\eta_2=0) = \frac{i\mu R(v)}{2\alpha_s}\Bigg\{&\frac{A_o}{\sqrt{|\eta_1|}} + \frac{1}{i\pi}\frac{2\alpha_s}{\mu R(v)} \\ &\cdot\frac{1}{\sqrt{|\eta_1|}}\int_{-L}^{0}\frac{\sqrt{|\xi|}\tau(\xi/L)}{\xi - |\eta_1|}d\xi\Bigg\}.\end{aligned} \tag{14}$$

Far ahead of the crack tip, i.e., for $\eta_1 = D \gg L$, $\eta_2 = 0$, the solution must match the square root singular stress intensity factor field (K_{II}^d field) for steady subsonic crack growth.

$$\sigma_{12}(\eta_1 = D, \eta_2 = 0) \approx \frac{\mu R(v)}{2\alpha_s}\frac{iA_o}{\sqrt{D}} = \frac{K_{II}^d}{\sqrt{2\pi D}}.$$

$$\Rightarrow iA_o = \frac{1}{\sqrt{2\pi}}\frac{K_{II}^d}{\mu}\frac{2\alpha_s}{R(v)}. \tag{15}$$

Also, with the presence of a cohesive zone the stresses must be bounded at its front end, and the stress intensity here should vanish.

$$\lim_{\eta_1 \to 0^+} \sigma_{12}(\eta_1 > 0, \eta_2 = 0)\sqrt{2\pi\eta_1} = 0. \tag{16a}$$

$$\Rightarrow iA_o = \frac{1}{\mu\pi}\frac{2\alpha_s}{R(v)}\int_{-L}^{0}\frac{\tau(\xi/L)}{\sqrt{|\xi|}}d\xi. \tag{16b}$$

$$\Rightarrow K_{II}^d = \sqrt{\frac{2}{\pi}}\int_{-L}^{0}\frac{\tau(\xi/L)}{\sqrt{|\xi|}}d\xi. \tag{16c}$$

The η_1 gradient of the sliding displacement u_1 along the upper cohesive surface is given by

$$u_{1,1}(-L < \eta_1 < 0, \eta_2 \to 0^+) = -\frac{v^2}{\beta^2}\frac{\alpha_s}{R(v)}\frac{\sqrt{|\eta_1|}}{\mu\pi}$$
$$\mathrm{pv}\int_{-L}^{0}\frac{\tau(\xi/L)}{\sqrt{|\xi|}(\xi + |\eta_1|)}d\xi, \tag{17}$$

where "pv" stands for Cauchy principal value (indicating that the integral must be interpreted in the Cauchy principal value sense). For steady crack growth, $(\dot{}) = -v(\ )_{,1}$. Hence the above result relates the rate of sliding within the cohesive zone to the cohesive traction resisting the sliding.

3.2. Intersonic Case, $\beta < v < \alpha$

[25] Owing to the symmetry of the problem, we consider the solution to equations (4) only in the upper half plane ($\eta_2 \geq 0$). The general solutions for the displacement potentials are [*Freund*, 1990]

$$\phi(\eta_1, \eta_2) = \mathrm{Re}\{F(z_l)\}, \tag{18a}$$

$$\psi(\eta_1, \eta_2) = g(\eta_1 + \hat{\alpha}_s\eta_2), \tag{18b}$$

where F is the same function as in the subsonic case and $g()$ is a real function of its argument. The radiation condition is employed here; that is, an intersonic crack is only capable of generating backward running shear waves. The displacement and stress fields may now be expressed in terms of the unknown functions F and g.

[26] Mode II symmetries ahead of the crack tip reduce to

$$F''^{+}(\eta_1) = -\bar{F}''^{-}(\eta_1) \qquad \eta_1 > 0, \tag{19a}$$

$$g''^{+}(\eta_1) = 0 \qquad \eta_1 > 0. \tag{19b}$$

[27] Following equation (19), we can define $\theta(z)$ (by analytic continuation), a function analytic everywhere on the complex z plane except on the crack faces as

$$\theta(z) = \begin{cases} F''(z) & \mathrm{Im}\{z\} \geq 0, \\ -\bar{F}''(z) & \mathrm{Im}\{z\} < 0. \end{cases} \tag{20}$$

The traction boundary conditions on the upper crack face and the cohesive surface reduce to

$$g''^{+}(\eta_1) = \frac{-\left(1 - \hat{\alpha}_s^2\right)}{4\hat{\alpha}_s}\left\{F''^{+}(\eta_1) + \bar{F}''^{-}(\eta_1)\right\} \qquad \eta_1 < 0, \tag{21a}$$

$$\mu\left[-2\alpha_l \mathrm{Im}\{F''^{+}(\eta_1)\} - \left(1 - \hat{\alpha}_s^2\right)g''^{+}(\eta_1)\right]$$
$$\begin{cases} = \tau(\eta_1/L) & -L < \eta_1 < 0, \\ 0 & \eta_1 < -L. \end{cases} \tag{21b}$$

The second equation of equation (20) reduces to

$$\left[\left(1 - \hat{\alpha}_s^2\right)^2 + 4i\alpha_l\hat{\alpha}_s\right]\theta^{+}(\eta_1) - \left[\left(1 - \hat{\alpha}_s^2\right)^2 - 4i\alpha_l\hat{\alpha}_s\right]\theta^{-}(\eta_1)$$
$$= \begin{cases} \frac{4\hat{\alpha}_s}{\mu}\tau(\eta_1/L) & -L < \eta_1 < 0, \\ 0 & \eta_1 < -L. \end{cases} \tag{22}$$

Similar to the subsonic case, the general solution for the inhomogeneous Hilbert problem in the upper half plane ($\eta_2 \geq 0$), is given by

$$\theta(z) = F''(z) = \frac{A_o}{z^q} + \frac{1}{2\pi i}\frac{4\hat{\alpha}_s}{\mu R_q}\frac{1}{z^q}\int_{-L}^{0}\frac{|\xi|^q\tau(\xi/L)}{\xi - z}d\xi, \tag{23}$$

where

$$q = \frac{1}{\pi}\tan^{-1}\left[\frac{4\alpha_l\hat{\alpha}_s}{\left(1 - \hat{\alpha}_s^2\right)^2}\right] \tag{24a}$$

$$R_q = \sqrt{16\alpha_l^2\hat{\alpha}_s^2 + \left(1 - \hat{\alpha}_s^2\right)^4}. \tag{24b}$$

From mode II symmetries we can readily conclude that A_o is pure imaginary.

[28] The shear stress ahead of the crack tip is given by

$$\sigma_{12}(\eta_1 > 0, \eta_2 = 0) = \frac{2\mu\alpha_l iA_o}{|\eta_1|^q}$$
$$+\frac{\sin q\pi}{\pi}\frac{1}{|\eta_1|^q}\int_{-L}^{0}\frac{|\xi|^q\tau(\xi/L)}{\xi - |\eta_1|}d\xi. \tag{25}$$

Far ahead of the crack tip, i.e., for $\eta_1 = D \gg L, \eta_2 = 0$, the solution must match the singular solution.

$$\sigma_{12}(\eta_1 = D, \eta_2 = 0) \approx \frac{2\mu\alpha_l iA_o}{D^q} = \frac{K_{II}^{*d}}{\sqrt{2\pi}D^q},$$

$$\Rightarrow iA_o = \frac{1}{\sqrt{2\pi}}\frac{K_{II}^{*d}}{2\mu\alpha_l}. \tag{26}$$

K_{II}^{*d} is the intersonic mode II stress intensity factor. Also, with the presence of a cohesive zone the stresses must be bounded at the front end, and the stress intensity factor here should vanish.

$$\lim_{\eta_1 \to 0^+} \sigma_{12}(\eta_1 > 0, \eta_2 = 0)\sqrt{2\pi}\,\eta_1^q = 0. \tag{27a}$$

$$\Rightarrow iA_o = \frac{1}{2\mu\alpha_l}\frac{\pi}{\sin q\pi}\int_{-L}^{0}\frac{\tau(\xi/L)}{|\xi|^{1-q}}d\xi. \tag{27b}$$

$$\Rightarrow K_{II}^{*d} = \sin q\pi\sqrt{\frac{2}{\pi}}\int_{-L}^{0}\frac{\tau(\xi/L)}{|\xi|^{1-q}}d\xi. \tag{27c}$$

The relation between the rate of sliding within the cohesive zone and the cohesive shear traction resisting the sliding is given by

$$u_{1,1}(-L < \eta_1 < 0, \eta_2 \to 0^+) = \frac{(1+\hat{\alpha}_s^2)\sin^2 q\pi}{4\pi\mu\alpha_l}\left\{\frac{\pi\tau(\eta_1/L)}{\tan q\pi}\right.$$

$$\left. -|\eta_1|^{1-q}\,\mathrm{pv}\int_{-L}^{0}\frac{\tau(\xi/L)}{|\xi|^{1-q}(\xi+|\eta_1|)}d\xi\right\}. \tag{28}$$

4. Velocity Weakening Cohesive Law

[29] Cohesive zones of the slip-weakening type have been used extensively in the past to model shear ruptures on earthquake faults [*Ida*, 1972; *Andrews*, 1976; *Burridge et al.*, 1979]. Slip-weakening models are an extension to shear faults of cohesive zone models initially introduced for tensile cracks by *Dugdale* [1960] to model plastic yielding in ductile materials and by *Barenblatt* [1962] to model interatomic cohesion in brittle solids. A slip-weakening law relates the shear traction on a cohesive surface to the local slip. The cohesive shear traction decays from some relatively high peak strength, necessary to get slip started, down to zero or some constant reduced stress, when the local slip becomes equal to a characteristic breakdown slip. For shear ruptures on fault planes, cohesive forces result from nonuniform frictional sliding occurring immediately behind the rupture front. According to the elastodynamic shear crack model, as the rupture front approaches a material particle along its path, the particle experiences a sudden jump in slip rate, which then decays rapidly behind the rupture front. Consequently, the frictional strength of the fault is assumed to decay behind the rupture front over a characteristic slip distance. Slip-weakening laws assume that the strength decay depends only on the local slip; however, rate- and state-dependent friction laws, which most materials seem to obey, indicate that the frictional strength should also depend strongly on the local slip rate [*Ruina*, 1983; *Rice and Ruina*, 1983; *Kilgore et al.*, 1993].

[30] It was mentioned before that intersonic mode II crack growth in our laboratory specimens is accompanied by a far-field negative mode I dynamic stress intensity factor (negative K_I^d). This results in crack face contact, with large negative normal tractions acting on the crack faces at distances close to the tip. Hence, in the vicinity of the tip, one might expect the crack faces to undergo nonuniform frictional sliding. On the basis of experimental data, *Ruina* [1983] and *Rice and Ruina* [1983] proposed that the sliding friction, apart from being proportional to the normal traction, is also a nonlinear function of slip rate and a number of internal variables that describe the local "state" of the sliding surfaces. The slip rates at distances close to the tip are very large (of the order of 1 to 10 m s^{-1}). Very limited data are available on dynamic friction at such high slip rates [*Prakash and Clifton*, 1992, 1993]. However, it is generally accepted that steady state frictional stress decreases with increasing slip rate. Hence a rate-dependent line cohesive zone may be used to model the finite zone in the vicinity of the crack tip, where nonuniform frictional sliding occurs. Here the cohesive constitutive relation represents a friction law, relating the frictional resistance (cohesive shear traction) to the local slip rate. Under the assumption of steady crack propagation, the dependence of sliding friction on local "state" may be neglected.

[31] Rate-dependent cohesive constitutive relations, which relate the traction on a cohesive surface to the local displacement rate, have been used in the past for modeling elastic-viscoplastic material behavior [*Glennie*, 1971a, 1971b; *Freund and Lee*, 1990]. However, in these investigations the assumed cohesive law models rate strengthening behavior. *Glennie* [1971a] analyzed the problem of a uniformly moving semi-infinite mode I crack in plane strain, with a rate-dependent cohesive zone in front of it. He used a strip yield zone, with the yield stress linearly dependent on strain rate to model thin plastic zones ahead of running mode I cracks in sheets of mild steel. He suggested that the increased resistance to plastic flow at high crack speeds can explain the relatively low terminal speeds observed for running mode I cracks. *Freund and Lee* [1990] analyzed the same problem and, to model the failure mode transition observed in some ferritic steels, introduced two different fracture criteria, one for ductile fracture based on a critical crack tip opening displacement and another for brittle fracture based on a critical stress in front of the tip. They investigated the dependence of the far-field applied stress intensity factor, crack speed, and a rate parameter on the failure mode selection.

[32] The rate-dependent cohesive law used by *Glennie* [1971a, 1971b] and *Freund and Lee* [1990] is adapted here for modeling the rate-dependent cohesive zone in the vicinity of a dynamic shear crack propagating along a weak plane. The cohesive constitutive relation, which relates the cohesive shear traction at any point within the cohesive zone to the local slip rate, was chosen to be of the form (see Figure 7b)

$$\tau(\dot{\delta}) = \tau_o\left[1 + \beta^*\frac{\mu}{2\tau_o}\frac{|\dot{\delta}|}{\beta}\right], \tag{29}$$

where τ_o is the cohesive shear strength of the material under quasi-static sliding, β^* is a dimensionless rate parameter (or velocity weakening parameter) and $\dot{\delta}(\eta_1/L) = \dot{u}_1(\eta_1/L, \eta_2 \to 0^+) - \dot{u}_1(\eta_1/L, \eta_2 \to 0^-)$ is the local slip rate. For slip rates $\dot{\delta}$ of the order of 10^1 m s^{-1} the dimensionless factor $\mu/(2\tau_o)$ in the above cohesive law ensures that β^* has the order of unity. For velocity weakening, β^* must be negative.

The shear cohesive strength decreases from τ_o at the front end of the cohesive zone and vanishes at the physical crack tip where the slip rate has a magnitude $(2\tau_o\beta)/(\mu|\beta^*|)$. Thus the cohesive shear traction at any point within the cohesive zone is given by

$$\tau\left(\frac{\eta_1}{L}\right) = \tau_o\left[1 + \beta^*\frac{\mu}{2\tau_o}\frac{|\dot{\delta}(\eta_1/L)|}{\beta}\right] \qquad -1 < \frac{\eta_1}{L} < 0. \quad (30)$$

The relative sliding displacement δ (or δ_1) at the mathematical crack tip ($\eta_1 = \eta_2 = 0$) is zero, and if we reasonably assume that back slipping is not permissible, then it should increase monotonically to δ_t, the crack tip sliding displacement, as the physical crack tip ($\eta_1 = -L, \eta_2 = 0$) is approached. Hence $\dot{\delta}(\eta_1/L) = -2v u_{1,1}(\eta_1/L, \eta_2 \rightarrow 0^+)$ must be nonnegative over the entire cohesive zone. We discuss the consequences of this "physical restriction" in section 5. From now on, we call the front end of the cohesive zone the mathematical crack tip and the rear end the physical crack tip.

[33] Using the constitutive assumption on the response within the cohesive zone as given in equation (30), a singular integral equation for the unknown cohesive traction distribution is obtained as follows. Substituting for $u_{1,1}$ from equations (17) and (28), we obtain

$$f(\eta_1) - \left\{\beta^*\frac{v^3}{\beta^3}\frac{\alpha_s}{R(v)}\right\}\frac{1}{\pi}\mathrm{pv}\int_{-L}^{0}\frac{f(\xi)}{(\xi + |\eta_1|)}d\xi = \frac{1}{\sqrt{|\eta_1|}}$$

$$0 \le v < \beta, \quad (31a)$$

$$\hat{f}(\eta_1)\left\{1 + \beta^*\frac{v^3}{\beta^3}\frac{\hat{\alpha}_s}{R_q}\cos q\pi\right\} - \left\{\beta^*\frac{v^3}{\beta^3}\frac{\hat{\alpha}_s}{R_q}\sin q\pi\right\}$$

$$\frac{1}{\pi}\mathrm{pv}\int_{-L}^{0}\frac{\hat{f}(\xi)}{(\xi + |\eta_1|)}d\xi = \frac{1}{|\eta_1|^{1-q}} \qquad \beta < v < \alpha, \quad (31b)$$

where

$$f(\eta_1) = \frac{\tau(\eta_1/L)}{\tau_o\sqrt{|\eta_1|}} \qquad 0 \le v < \beta \quad (32a)$$

$$\hat{f}(\eta_1) = \frac{\tau(\eta_1/L)}{\tau_o|\eta_1|^{1-q}} \qquad \beta < v < \alpha. \quad (32b)$$

[34] Equation (31) is a pair of singular integral equations of the Cauchy type, the solutions to which, subject to the boundary conditions

$$\tau(\eta_l \rightarrow 0^-) \rightarrow \tau_o,$$

$$\sqrt{1 + \eta_l}\,\tau(\eta_l \rightarrow -1^+) \rightarrow 0 \qquad 0 \le v < \beta \quad (33)$$

$$\tau(\eta_l \rightarrow 0^-) \rightarrow \tau_o,$$

$$(1 + \eta_l)^q\tau(\eta_l \rightarrow -1^+) \rightarrow 0 \qquad \beta < v < \alpha, \quad (34)$$

give the unknown cohesive traction distributions, $\tau(-1 < \eta_1/L < 0)$ for the subsonic and intersonic cases respectively. Here $\eta_1 = \eta_1/L$. The solution procedure is given in Appendix A.

5. Solution

[35] The cohesive shear traction distribution is given by (see Appendix A)

$$\frac{\tau}{\tau_o} = \begin{cases} 1 + \dfrac{\sin\gamma\pi}{\pi}\dfrac{(-\eta_1/L)^{\gamma+1/2}}{(1+\eta_1/L)^{\gamma}} \\ \quad \displaystyle\int_0^1 \frac{(1-s)^{\gamma}}{\sqrt{s}(1+s\,\eta_1/L)}ds & 0 \le v < c_R, \\ 1 + \dfrac{\sin\lambda\pi}{\pi}\dfrac{(-\eta_1/L)^{1-q+\lambda}}{(1+\eta_1/L)^{\lambda}} \\ \quad \displaystyle\int_0^1 \frac{(1-s)^{\lambda}}{s^q(1+s\,\eta_1/L)}ds & \beta < v < \alpha. \end{cases} \quad (35)$$

where

$$\gamma = \frac{1}{\pi}\tan^{-1}\left\{\beta^*\frac{v^3}{\beta^3}\frac{\alpha_s}{R(v)}\right\} \qquad 0 \le v < c_R, \quad (36)$$

$$\lambda = \frac{1}{\pi}\tan^{-1}\left\{\frac{\beta^*\frac{v^3}{\beta^3}\frac{\hat{\alpha}_s}{R_q}\sin q\pi}{1 + \beta^*\frac{v^3}{\beta^3}\frac{\hat{\alpha}_s}{R_q}\cos q\pi}\right\} \qquad \beta < v < \alpha, \quad (37)$$

and the integrals in equation (35) converge for $-1 \le \eta_1/L \le 0$. As mentioned before, the crack speed regime $c_R < v < \beta$ is inadmissible for running mode II cracks from energetic considerations, and henceforth we restrict ourselves to sub-Rayleigh ($0 \le v < c_R$) and intersonic regimes only.

[36] For velocity weakening, $\beta^* < 0$, and by taking the limit $\eta_1 \rightarrow -L$ in equation (35), we can readily conclude that τ/τ_o vanishes at the physical crack tip. It is shown (see Figure 10) that with $\beta^* < 0$, τ decreases monotonically from τ_o at $\eta_1 = 0$ and vanishes at the physical crack tip ($\eta_1 \rightarrow -L$), for both sub-Rayleigh and intersonic crack speeds. Moreover, frictional sliding requires that the cohesive shear traction (frictional resistance) must always oppose the relative sliding between the cohesive surfaces. Hence the relative slip between the cohesive surfaces must always be positive (no back slipping) and the slip rate $_1$ must be nonnegative over the entire cohesive zone. Hence solution (35) is admissible, provided

$$\frac{\dot{\delta}_1}{\beta}(-L < \eta_1 < 0) \ge 0. \quad (38)$$

Combining equations (35) and (30), an expression for the slip rate in terms of the crack speed v and the weakening parameter β^* can be obtained. For $-L < \eta_1 < 0$,

$$\frac{\dot{\delta}_1}{\beta} = \begin{cases} \dfrac{2}{\beta^*}\dfrac{\tau_o}{\mu}\dfrac{\sin\gamma\pi}{\pi}\dfrac{(-\eta_1/L)^{\gamma+1/2}}{(1+\eta_1/L)^{\gamma}} \\ \quad \displaystyle\int_0^1 \frac{(1-s)^{\gamma}}{\sqrt{s}(1+s\,\eta_1/L)}ds & 0 \le v < c_R, \\ \dfrac{2}{\beta^*}\dfrac{\tau_o}{\mu}\dfrac{\sin\lambda\pi}{\pi}\dfrac{(-\eta_1/L)^{1-q+\lambda}}{(1+\eta_1/L)^{\lambda}} \\ \quad \displaystyle\int_0^1 \frac{(1-s)^{\lambda}}{s^q(1+s\,\eta_1/L)}ds & \beta < v < \alpha. \end{cases} \quad (39)$$

From equations (39) for slip rate, we can conclude that for velocity weakening cohesive zones ($\beta^* < 0$) the required

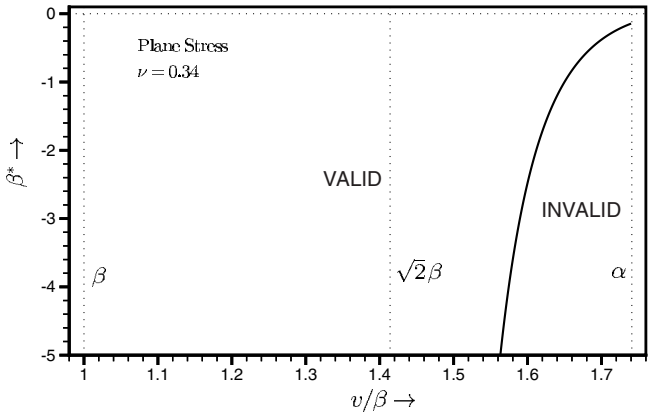

Figure 8. Region of validity of the velocity weakening solution in the $\beta^* - v/\beta$ space. Note for $-0.141228 < \beta^* < 0$, the velocity weakening solution is valid for the entire sub-Rayleigh as well as the intersonic regime. For $\beta^* < -0.141228$, a small velocity regime close to α becomes inadmissible.

condition (38) is satisfied for all $0 \leq v < c_R$, but for intersonic crack speeds it is satisfied only over a portion of the $\beta^* - v/\beta$ space. In particular, for $\beta^* < 0$ and $\beta < v < \alpha$, equation (38) is satisfied if

$$1 + \beta^* \frac{v^3}{\beta^3} \frac{\hat{\alpha}_s}{R_q} \cos q\pi > 0. \tag{40}$$

An alternate way of arriving at the same condition as above is by imposing a physical restriction that energy must be dissipated and not generated over any part of the velocity weakening cohesive zone, i.e.,

$$\frac{1}{v} \int_{\eta^*}^{\eta^* + d\eta^*} \tau(\eta_1) \dot{\delta}_1(\eta_1) d\eta_1 \geq 0, \tag{41}$$

for every η^* such that $-L < \eta^* < 0$. Since $\tau(-L < \eta_1 < 0) \geq 0$ (according to equation (35)) everywhere in the cohesive zone, the above condition implies that $\dot{\delta}_1$ is nonnegative over the entire cohesive zone. For the sub-Rayleigh speed regime this condition is satisfied for all $\beta^* \leq 0$. However, for intersonic crack speeds, such a condition is satisfied only if equation (40) is met.

[37] Figure 8 shows a curve in the $\beta^* - v/\beta$ space that delineates the region of validity of the solution (35) for an intersonic mode II crack with a velocity weakening cohesive zone. Moderate values of β^* up to -5 are chosen. The energetic requirement (40) is satisfied for most of the intersonic regime, except for crack speeds close to α. For plane stress and with $\nu = 0.34$ (conditions of our laboratory experiments), there exists a small range, $-0.149 < \beta^* \leq 0$, where the solution (35) is valid over the entire intersonic regime. With decreasing β^* the solution becomes invalid over more and more of the intersonic regime, and as $\beta^* \rightarrow -\infty$, at only one intersonic speed equal to $\sqrt{2}\,\beta$, is equation (40) satisfied. This can be readily expected, since the solution (35) at $v = \sqrt{2}\,\beta$ behaves "subsonic-like." As mentioned before, the unknown weakening parameter β^* is expected to be of the order "unity," and hence in the intersonic regime the velocity weakening cohesive zone model presented here is likely to be inadmissible only over a very small speed regime close to α. Similar to Figure 8, the remaining figures in this paper are all plotted for 2-D plane stress and for $\nu = 0.34$ (Poisson's ratio of Homalite-100) so as to be comparable with the experimental observations described in section 2.

[38] Figure 9a shows the variation of γ with crack speed (sub-Rayleigh) for different values of the weakening parameter β^*. Figure 9b is a similar plot of λ for intersonic crack speeds. With a velocity weakening cohesive zone ($\beta^* < 0$) the shear stress vanishes at the physical crack tip. From equation (35) we see that γ and λ are the indices measuring the rate of decay of τ as the physical crack tip is approached. $-1/2 < \gamma < 0$ for sub-Rayleigh crack speeds and $-1/2 < \lambda < 0$ for intersonic crack speeds. Both these indices are strong functions of v and β^*. The lower the γ (or λ), the faster the cohesive shear traction decays as the physical crack tip is approached. Hence from Figure 9 we see that lower β^* and higher v would result in a faster decay of the cohesive shear stress. For the trivial case with $\beta^* = 0$, the cohesive law becomes rate independent (of the Dugdale type) and both γ and λ reduce to zero.

[39] With the known cohesive shear traction equation (35), one can compute F'', G'', and g'' and thus obtain the

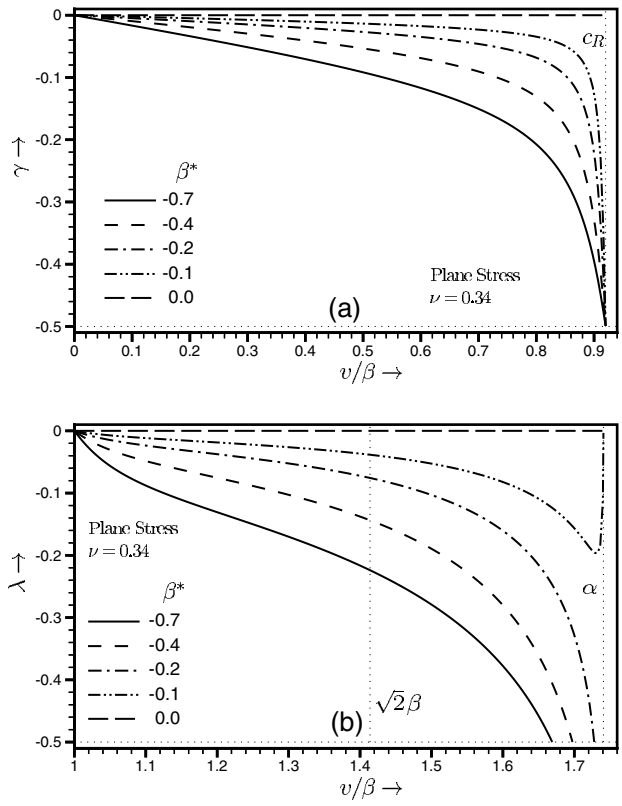

Figure 9. Dynamic in-plane shear crack with a velocity weakening cohesive zone; exponent characterizing the decay of cohesive shear traction. (a) Subsonic speeds for different values of the weakening parameter β^*. (b) Intersonic speeds for different values of the weakening parameter β^*.

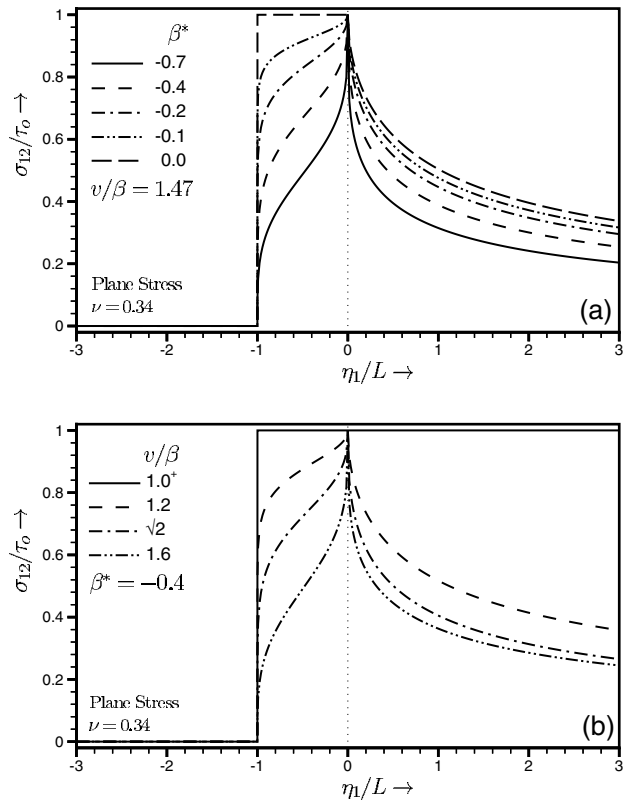

Figure 10. Intersonically propagating mode II crack with a velocity weakening cohesive zone. (a) Stress component σ_{12} on the crack plane for $v/\beta = 1.47$ and for different values of the weakening parameter β^*. (b) Stress component σ_{12} on the crack plane for $\beta^* = -0.4$ and for different values of crack tip speed v.

dominant near-tip stress field. The stress field is given in Appendix B for both sub-Rayleigh and intersonic crack speeds. For mode II cracks with a velocity weakening cohesive zone, σ_{12} on the crack plane ($\eta_2 \to 0^+$), ahead of the mathematical crack tip, is given by

$$\frac{\sigma_{12}}{\tau_o}(\eta_1/L > 0) = \frac{1}{\pi}\sqrt{\frac{\eta_1}{L}}\left[\int_0^1 \frac{d\xi}{\sqrt{\xi}(\xi + \eta_1/L)} + \int_0^1 \frac{ds}{\sqrt{s}(1 + s\,\eta_1/L)} - \left(\frac{\eta_1/L}{1+\eta_1/L}\right)^{\gamma}\int_0^1 \frac{(1-s)^{\gamma}}{\sqrt{s}(1+s\,\eta_1/L)}ds\right], \quad (42)$$

for $0 \le v < c_R$ and

$$\frac{\sigma_{12}}{\tau_o}(\eta_1/L > 0) = \frac{\sin q\pi}{\pi}\left(\frac{\eta_1}{L}\right)^{1-q}\left\{\int_0^1 \frac{d\xi}{\xi^{1-q}(\xi + \eta_1/L)} + \int_0^1 \frac{ds}{s^q(1 + s\,\eta_1/L)} - \left(\frac{\eta_1/L}{1+\eta_1/L}\right)^{\lambda}\int_0^1 \frac{(1-s)^{\lambda}}{s^q(1+s\,\eta_1/L)}\,ds\right\}, \quad (43)$$

for $\beta < v < \alpha$. The parameter σ_{12} within the cohesive zone is given in equation (35), and it vanishes on the crack faces. The crack plane shear stress distribution is shown in Figure 10a for different values of β^* at a fixed intersonic speed, $v = 1.47\,\beta$ (later on we compare the isochromatic fringe pattern predicted by the model with an experimentally recorded pattern at this particular intersonic speed). Similarly, Figure 10b shows the crack plane shear stress distribution for different intersonic speeds at a fixed $\beta^* = -0.4$ (It will be shown later that β^* for our laboratory specimens is close to -0.4 and is obtained by comparing the model predictions with the experimental observations). From Figure 10 we confirm our expectation that a velocity weakening law results in a cohesive traction that decays from its maximum value of τ_o at the mathematical crack tip and vanishes at the physical crack tip. As mentioned above, we see that a lower β^* or a faster v results in a faster decay of the cohesive shear traction. Unlike *Freund*'s [1979] singular solution, we find that σ_{12} is bounded all along the crack plane. Far ahead of the tip ($\eta_1 \gg L$), the singular solution for a sharp crack is recovered.

[40] The crack plane distribution of the direct stress component σ_{11} is shown in Figure 11. On the crack plane ($\eta_2 \to 0^+$),

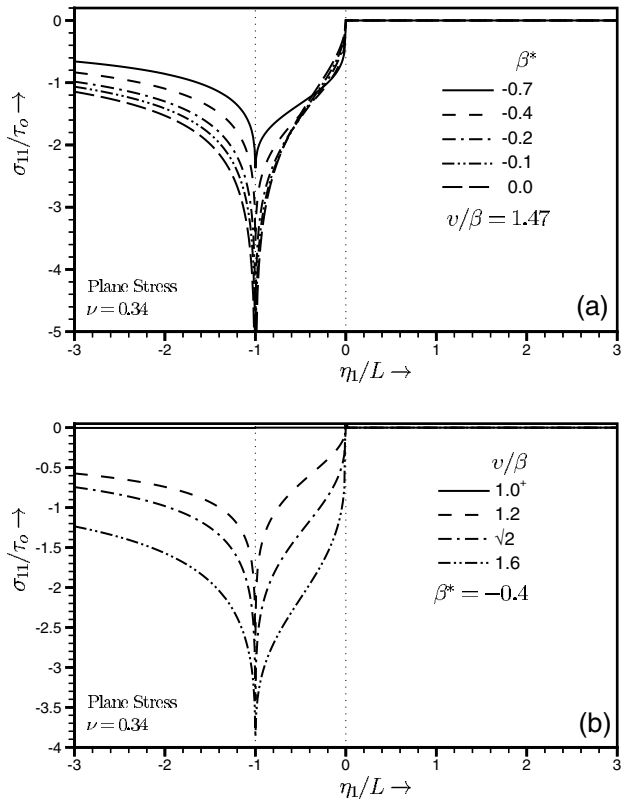

Figure 11. Intersonically propagating mode II crack with a velocity weakening cohesive zone. (a) Stress component σ_{11} on the crack plane for $v/\beta = 1.47$ and for different values of the weakening parameter β^*. (b) Stress component σ_{11} on the crack plane for $\beta^* = -0.4$ and for different values of crack tip speed v.

$$\frac{\sigma_{11}}{\tau_o}(-1<\eta_l<0)=\frac{\left(\alpha_l^2+\hat{\alpha}_s^2\right)}{\alpha_l}\frac{\sin^2 q\pi}{\pi}\left[\frac{\pi}{\tan q\pi}+\left(\frac{-\eta_1}{L}\right)^{1-q}\cdot\left\{\mathrm{pv}\int_0^1\frac{d\xi}{\xi^{1-q}(\xi+\eta_1/L)}+\int_0^1\frac{ds}{s^q(1+s\,\eta_1/L)}\right\}+\sin\lambda\pi\,\frac{(-\eta_1/L)^{1-q+\lambda}}{(1+\eta_1/L)^{\lambda}}\left\{\frac{1}{\tan q\pi}-\frac{1}{\tan\lambda\pi}\right\}\cdot\int_0^1\frac{(1-s)^{\lambda}}{s^q(1+s\,\eta_1/L)}ds\right],\tag{44a}$$

$$\frac{\sigma_{11}}{\tau_o}(\eta_l<-1)=\frac{\left(\alpha_l^2+\hat{\alpha}_s^2\right)}{\alpha_l}\frac{\sin^2 q\pi}{\pi}\left(\frac{-\eta_1}{L}\right)^{1-q}\cdot\left[\int_0^1\frac{d\xi}{\xi^{1-q}(\xi+\eta_1/L)}\int_0^1\frac{ds}{s^q(1+s\eta_1/L)}-\left(\frac{\eta_1/L}{1+\eta_1/L}\right)^{\lambda}\int_0^1\frac{(1-s)^{\lambda}}{s^q(1+s\,\eta_1/L)}ds\right],\tag{44b}$$

for $\beta<v<\alpha$. Also, $\sigma_{11}(\eta_1/L>0)=0$. For a shear crack with a velocity weakening cohesive zone ($\beta^*<0$), σ_{11} is bounded all along the crack plane and attains a finite extremum at the physical crack tip, whereas for a shear crack with a Dugdale-type cohesive zone ($\beta^*=0$), σ_{11} is singular at the physical crack tip, with the strength of the singularity less than q (logarithmic singularity for sub-Rayleigh speeds). Figure 11a shows the crack plane distribution of σ_{11} for different β^* at a fixed intersonic speed, $v=1.47\beta$. On the other hand, Figure 11b shows the crack plane distribution of σ_{11} for different intersonic speeds at a fixed $\beta^*=-0.4$. It must be noted here that the nature of loading in our experiments (as described in section 2) is such that the far-field dynamic mode II stress intensity factor associated with the propagating crack is negative. This results in σ_{11} to be positive in the upper half plane ($\eta_2>0$) and negative in the lower half. However, the analytical solution (44) follows the conventional approach by assuming the far-field dynamic stress intensity factor to be positive, resulting in σ_{11} being compressive in the upper half plane.

[41] The cohesive zone length L is determined by imposing a physical requirement that the stress intensity at the front end of the cohesive zone should vanish. Incorporating the known traction distribution from equation (35) into equations (16c) and (27c), we obtain the length of the cohesive zone in terms of the far-field applied loading, shear strength of the crack plane τ_o, v, and β^*. Since the definition of stress intensity factor varies from sub-Rayleigh to intersonic speeds, we choose σ_{12}^D as the measure of the amplitude of far-field applied loading. The parameter σ_{12}^D is the "remote" shear stress on the crack plane a distance $D\gg L$ ahead of the crack tip, where the usual singular solution for the case of a mathematically sharp crack with no cohesive zone is expected to apply. The parameter σ_{12}^D is related to the subsonic and intersonic stress intensity factors as

$$\sigma_{12}^D=\sigma_{12}(\eta_1=D,\eta_2=0)=\begin{cases}\frac{K_{II}^d}{\sqrt{2\pi D}} & 0\le v<c_R,\\ \frac{K_{II}^{*d}}{\sqrt{2\pi D^q}} & \beta<v<\alpha.\end{cases}\tag{45}$$

The normalized cohesive zone length is given by

$$\frac{L}{L_o}=\begin{cases}\frac{1}{\pi}\left[\frac{\Gamma(\gamma+1/2)}{\Gamma(\gamma+1)}\right]^2 & 0\le v<c_R,\\ \frac{4}{\pi^2}\left(\frac{q\pi}{\sin q\pi}\right)^{1/q}\left(\frac{\sigma_{12}^D}{\tau_o}\right)^{1/q-2}\cdot\left[\frac{\Gamma(\lambda-q+1)}{\Gamma(1-q)\Gamma(1+\lambda)}\right]^{1/q} & \beta<v<\alpha,\end{cases}\tag{46}$$

where $\Gamma()$ is the standard Euler gamma function. The normalizing parameter L_o is the length of the cohesive zone associated with a quasi-statically growing mode II crack with the same far-field applied loading σ_{12}^D. It is given by

$$L_o=\frac{\pi^2}{4}\left(\frac{\sigma_{12}^D}{\tau_o}\right)^2 D.\tag{47}$$

In effect, L/L_o represents the parametric dependence of the cohesive zone length on v, β^*, and τ_o under a constant σ_{12}^D.

[42] For a propagating mode II crack with a Dugdale-type cohesive zone ($\beta^*=0$), L/L_o is independent of v and τ_o for sub-Rayleigh crack speeds, whereas it is a strong function of both v and τ_o for intersonic crack speeds. For sub-Rayleigh crack speeds where the singularity exponent (for a sharp crack with no cohesive zone) is a constant (= 1/2), the cohesive zone length remains constant at its quasi-static value. For intersonic speeds the dependence of L/L_o on v is similar to the dependence of q on v. L/L_o increases from 0 at β to a maximum of 1 at $\sqrt{2}\,\beta$ and thereafter decreases to 0 at α. For intersonic speeds, L/L_o is also a function of τ_o, with lower τ_o resulting in a higher cohesive zone size. For velocity weakening ($\beta^*<0$), L/L_o increases with crack speed and becomes unbounded as $v\to c_R$ ($\gamma\to-1/2$). For intersonic speeds the dependence of L/L_o on v at any β^* is similar to the case of $\beta^*=0$, except that the peak cohesive zone size is achieved at a speed higher than $\sqrt{2}\,\beta$. Also, as may be expected, lower β^* results in an increase in cohesive zone length. The dependence of L/L_o on shear strength of the crack plane τ_o, at any β^* is similar to the case of $\beta^*=0$, as discussed above.

[43] The distribution of sliding rate (or slip rate) $\dot{\delta}_1$ within the cohesive zone is given in equation (39) for both sub-Rayleigh and intersonic crack speeds. From equation (39) we see that the slip rate at any point in the cohesive zone is directly proportional to the shear strength of the crack plane τ_o. The slip rate distribution is also dependent on v and β^* in a complicated way. We examine the dependence of slip rate distribution within the cohesive zone on v and β^* at a constant value of μ/τ_o, chosen to be 136, which is equal to the ratio of shear modulus of Homalite (1.9 GPa) and the shear strength of the Homalite/Homalite bond ($\sim$14 MPa). Figure 12a shows the influence of rate sensitivity on the distribution of $\dot{\delta}_1$ for a representative sub-Rayleigh speed, $v=0.6\beta$. On the other hand, Figure 12b shows the variation of $\dot{\delta}_1$ within the cohesive zone for various sub-Rayleigh speeds at a fixed $\beta^*=-0.4$. For $\beta^*<0$, $\dot{\delta}_1$ increases monotonically from 0 at the mathematical crack tip and attains a finite, bounded maximum at the physical crack tip. This is the slip rate at which the cohesive shear strength vanishes in the velocity weakening model. Only for the case of $\beta^*=0$ (Dugdale-type cohesive zone), does $\dot{\delta}_1$ becomes

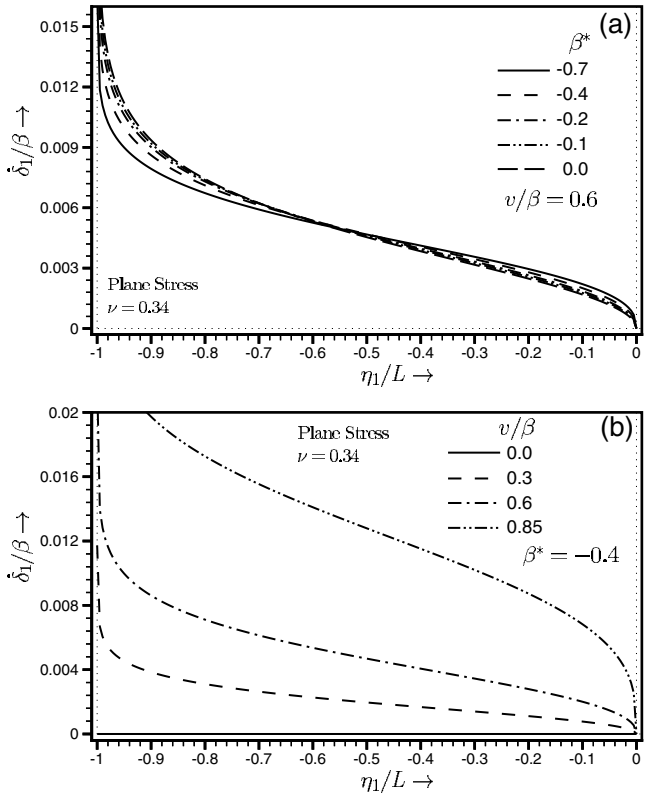

Figure 12. Subsonically propagating mode II crack with a velocity weakening cohesive zone. (a) Relative sliding rate $\dot{\delta}_1$ on the crack plane for $v/\beta = 0.6$ and for different values of the weakening parameter β^*. (b) Relative sliding rate $\dot{\delta}_1$ on the crack plane for $\beta^* = -0.4$ and for different values of the crack tip speed v.

unbounded at the physical crack tip. It can be clearly discerned from Figure 12 that the distribution of $\dot{\delta}_1$ in the cohesive zone exhibits a rather weak dependence on β^*, where as the dependence on v is very strong. As $v \to c_R$, $\dot{\delta}_1$ becomes unbounded through out the cohesive zone.

[44] Similarly, Figure 13a shows the influence of β^* on the variation of $\dot{\delta}_1$ within the cohesive zone for a chosen intersonic speed, $v = 1.47\beta$, and Figure 13b shows the variation of $\dot{\delta}_1$ within the cohesive zone for different intersonic speeds at a fixed $\beta^* = -0.4$. Similar to the sub-Rayleigh case, for $\beta^* < 0$, $\dot{\delta}_1$ is nonsingular and attains a finite maximum at the physical crack tip. The effect of β^* on $\dot{\delta}_1$ is rather small, though a bit more pronounced than in the sub-Rayleigh case. $\dot{\delta}_1 = 0$, everywhere in the cohesive zone for $v \to \beta,\alpha$ but is strongly influenced by v at all other intersonic speeds. It may be noted that through most of the cohesive zone, $\dot{\delta}_1$ is $\sim$2% of β for sub-Rayleigh speeds and is $\sim$4% of β for intersonic speeds. Two to four percent of β corresponds to sliding rates of up to a few tens of meters per second, consistent with our expectation while choosing the cohesive law. Note that these slip rates are comparable to those observed in earthquake ruptures [*Heaton*, 1990; *Ben-Zion*, 2001].

[45] The dynamic energy release rate G, defined as energy flux into the cohesive zone per unit crack advance per unit thickness along the crack front, may be expressed as

$$G = 2\int_0^{-L} \sigma_{12}(\eta_1, \eta_2 \to 0^+) u_{1,1}(\eta_1, \eta_2 \to 0^+) d\eta_1. \qquad (48)$$

For a steadily propagating mode II crack with a velocity weakening cohesive zone, the shear traction acting on the upper cohesive surface is given in equation (35) and the displacement gradient $u_{1,1}$ here is given in equations (17) and (28). Thus we obtain

$$\frac{G}{G_o} = \begin{cases} \dfrac{1}{\beta^*}\dfrac{(\alpha_l^2 - \alpha_s^2)}{v^3/\beta^3}\left[\dfrac{\Gamma(\gamma + 1/2)}{\Gamma(1+\gamma)}\right]^2 g(\gamma) & 0 \le v < c_R, \\ \dfrac{4}{\pi}\dfrac{1}{\beta^*}\dfrac{(\alpha_l^2 + \hat{\alpha}_s^2)}{v^3/\beta^3}\left(\dfrac{q\pi}{\sin q\pi}\right)^{1/q}\left(\dfrac{\sigma_{12}^D}{\tau_o}\right)^{1/q-2} & \\ \cdot\left[\dfrac{\Gamma(\lambda - q + 1)}{\Gamma(1-q)\Gamma(1+\lambda)}\right]^{1/q} g^*(\lambda, q) & \beta < v < \alpha, \end{cases} \qquad (49)$$

where

$$g(\gamma) = 2\gamma + \frac{\sin^2 \gamma\pi}{\pi^2}\int_0^1 \frac{\xi^{2\gamma+1}}{(1-\xi)^{2\gamma}}\left[\int_0^1 \frac{(1-s)^\gamma}{\sqrt{s}(1-s\xi)} ds\right]^2 d\xi, \qquad (50a)$$

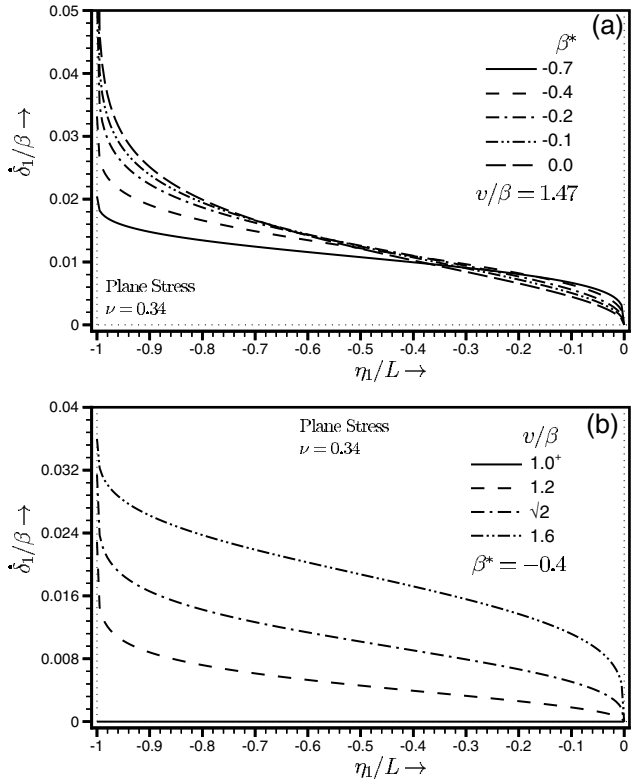

Figure 13. Intersonically propagating mode II crack with a velocity weakening cohesive zone. (a) Relative sliding rate $\dot{\delta}_1$ on the crack plane for $v/\beta = 1.47$ and for different values of the weakening parameter β^*. (b) Relative sliding rate $\dot{\delta}_1$ on the crack plane for $\beta^* = -0.4$ and for different values of the crack tip speed v.

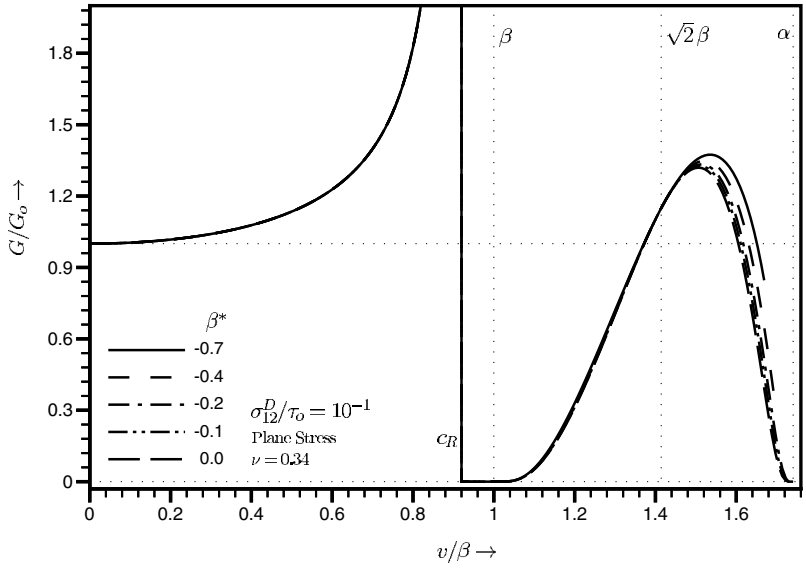

Figure 14. Dynamically propagating mode II crack with a velocity weakening cohesive zone. Dependence of dynamic energy release rate on the crack tip speed v, plotted for $\sigma_{12}^D/\tau_o = 10^{-1}$ and for different values of the weakening parameter β^*.

$$g^*(\lambda, q) = \frac{\lambda}{1-q} + \frac{\sin^2 \lambda\pi}{\pi^2} \int_0^1 \frac{\xi^{2-2q+2\lambda}}{(1-\xi)^{2\lambda}} \left[\int_0^1 \frac{(1-s)^\lambda}{s^q(1-s\xi)} ds \right]^2 d\xi, \tag{50b}$$

and G_o is the energy release rate associated with a quasi-statically propagating mode II crack with the same far-field load σ_{12}^D. Hence G/G_o represents the dependence of the dynamic energy release rate on v, β^*, and τ_o under a constant σ_{12}^D. G_o is given by

$$G_o = \frac{\pi(\kappa+1)}{4} \frac{\sigma_{12}^{D\,2} D}{\mu}, \tag{51}$$

where $\kappa = 3-4\nu$ for plane strain and $\kappa = (3-\nu)/(1+\nu)$ for plane stress.

[46] For steady sub-Rayleigh crack growth, G is independent of the process zone characteristics (i.e., G is independent of β^* and τ_o), and hence it is also equal to that in the case of a point sized process zone (sharp crack). Thus G/G_o is path-independent and hence is also equal to $2\alpha_s(\alpha_l^2 - \alpha_s^2)/R(v)$. This is reflected in Figure 14 which shows the variation of G/G_o with crack speed for different β^* at a constant value of $\sigma_{12}^D/\tau_o = 0.1$ and also in Figure 15 which shows the variation of G/G_o with crack speed for different σ_{12}^D/τ_o at a fixed $\beta^* = -0.4$. However, for intersonic speeds, G is dependent on the size and characteristics of the process zone. It depends on the extent of the process region as $(L/D)^{1-2q}$, where L is the cohesive zone size and D is the distance at which *Freund*'s [1979] singular solution dominates. As seen from Figures 14 and 15, the dynamic energy release rate G is finite through out the intersonic regime. It vanishes at crack speeds close to β and α. Hence, on the basis of the requirement of a positive energy flux the entire intersonic regime is admissible for mode II crack growth. In contrast, with a point sized process zone, G is zero everywhere in the intersonic regime except at $v = \sqrt{2}\,\beta$. The variation of G/G_o for intersonic speeds depends strongly on the shear strength of the fracture plane τ_o (see Figure 15). However, as seen from Figure 14, the influence of β^* is rather small. As $\tau_o \rightarrow \infty$, the singular solution with no cohesive zone is recovered and once again there exists only one intersonic speed $v = \sqrt{2}\,\beta$, at which the dynamic energy release rate is finite (see Figure 15). With a lower shear strength, more of the intersonic regime becomes admissible, the energy flux into the crack tip increases, and also the energy flux attains its peak at a speed higher than $\sqrt{2}\,\beta$. At $v = \sqrt{2}\,\beta$, an intersonic crack behaves "subsonic like"; that is, the explicit dependence on τ_o and β^* disappears, with G attaining a constant value equal to $2G_o/\sqrt{(1+\kappa)(3-\kappa)}$.

6. Secondary Tensile Cracks

[47] Intersonic mode II crack growth in our laboratory specimens was found to induce tensile cracking in the upper half of the specimen. Remarkably, these secondary tensile cracks were all found to be almost parallel to each other with their angle of inclination (with the normal to the crack plane) θ^* varying between 8° to 13°, with an average of ~10.6. In section 2, experimental evidence of the secondary cracks was presented, and a plausible scenario leading to their initiation, growth, and arrest was discussed. These secondary opening cracks originated a finite, but small distance (~1–2 mm) behind the main intersonic shear crack tip. It was argued in section 2 that the driving force leading to their initiation is provided by the near tip field associated with the main intersonic shear crack. Here we will use the near tip fields for a propagating mode II crack with a velocity weakening cohesive zone, in conjunction with the maximum principal tensile stress criterion for brittle fracture, to determine the feasibility of secondary crack initiation and, if possible, to extract some of the unknown model parameters for our laboratory specimens. Because of the

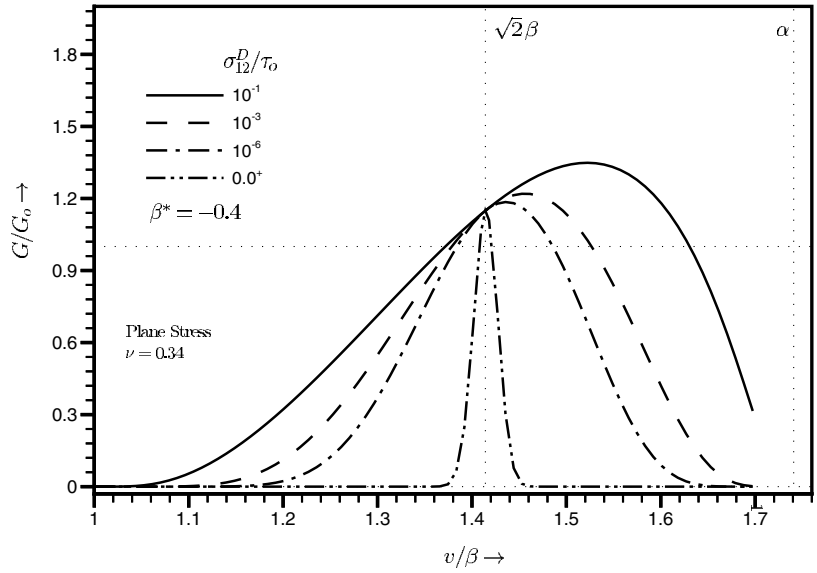

Figure 15. Dynamically propagating mode II crack with a velocity weakening cohesive zone. Dependence of dynamic energy release rate on the crack tip speed v, plotted for $\beta^* = -0.4$ and for different values of σ_{12}^D/τ_o.

nature of the applied loading in our experiments the far-field mode II stress intensity factor acting on the propagating intersonic mode II crack is negative. Hence, to be consistent with the experimental conditions, we change the sign of the remote shear load (σ_{12}^D) in the current section, which results in a change in the sign of cohesive shear tractions as well.

[48] The stress state at every point on the upper cohesive surface ($-L < \eta_1 < 0$, $\eta_2 \rightarrow 0^+$) is such that the shearstress component σ_{12} is negative and the direct stress component σ_{11} is positive (tensile). Note that $\sigma_{22} = 0$ on the upper cohesive surface. A simple Mohr's circle analysis yields the result that the maximum principal stress at every point on the upper cohesive surface is invariably tensile. Moreover, the minimum principal tensile stress is invariably compressive. The maximum principal tensile stress at any point on the upper cohesive surface is given by

$$\sigma_1(-L < \eta_1 < 0, \eta_2 \rightarrow 0^+) = \frac{\sigma_{11}}{2} + \sqrt{\left(\frac{\sigma_{11}}{2}\right)^2 + \sigma_{12}^2}, \qquad (52)$$

and the angle of inclination of the principal plane (its normal) with the horizontal (see Figure 5b) at any point on the upper cohesive surface is given by

$$\theta^*(-L < \eta_1 < 0, \eta_2 \rightarrow 0^+) = \frac{1}{2}\tan^{-1}\left(\frac{-2\sigma_{12}}{\sigma_{11}}\right). \qquad (53)$$

For a steadily propagating intersonic mode II crack with a velocity weakening cohesive zone, $\sigma_{12}(-L < \eta_1 < 0, \eta_2 \rightarrow 0^+) = -\tau(\eta_1/L)$, which is given in equation (35) and σ_{11} on the upper cohesive surface is given in equation (44) with the opposite sign. Thus σ_1 and θ^* on the upper cohesive surface may be obtained.

[49] Figure 16a show the distribution of the maximum principal tensile stress σ_1 along the upper cohesive surface for different intersonic speeds, at a fixed $\beta^* = -0.4$. The parameter σ_1 increases monotonically from zero at the mathematical crack tip and attains a finite maximum as the physical crack tip is approached ($\eta_1 \rightarrow -L$). This distribution is similar for other $\beta^* < 0$. If we assume that

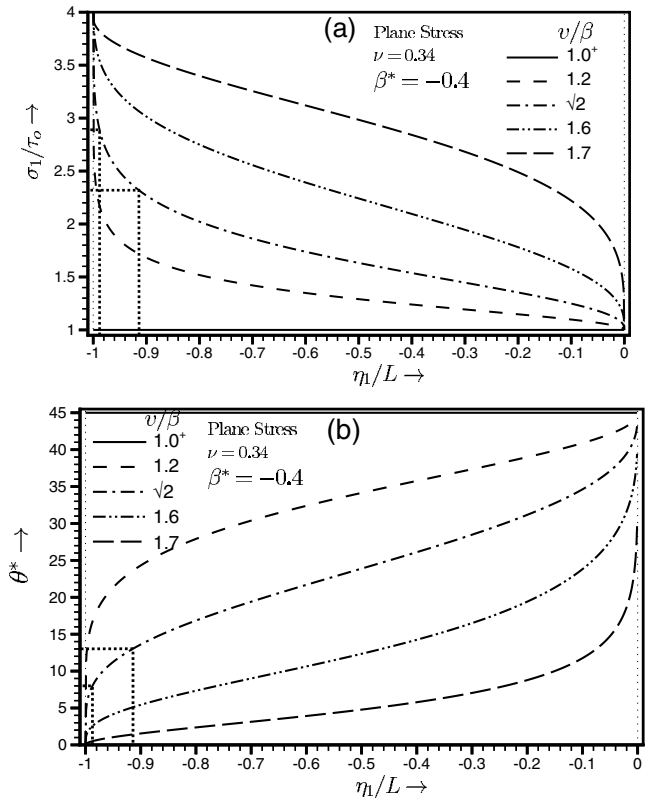

Figure 16. Dynamically propagating mode II crack with a velocity weakening cohesive zone. (a) Maximum principal tensile stress σ_1 on the upper cohesive surface for $\beta^* = -0.4$. (b) Inclination θ^* of the principal plane to the vertical for $\beta^* = -0.4$.

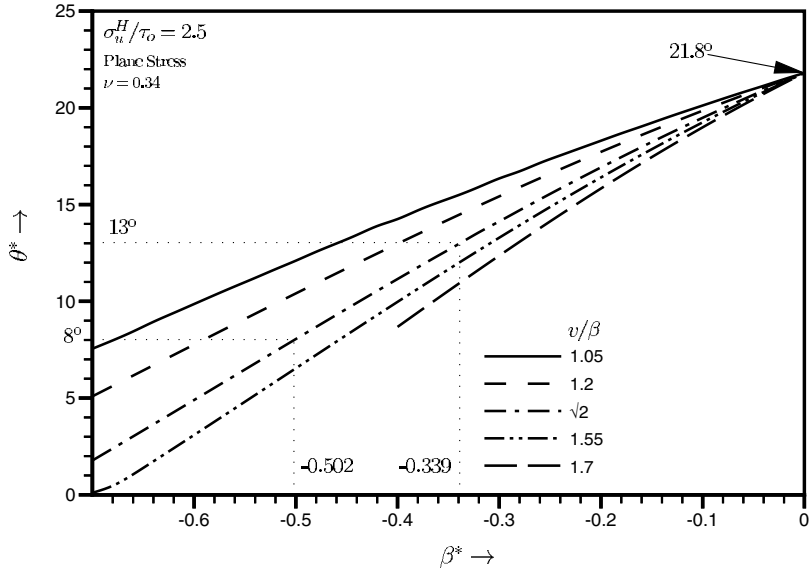

Figure 17. Dynamically propagating mode II crack with a velocity weakening cohesive zone. Predicted inclination of the secondary tensile cracks with the vertical, as a function of the weakening parameter β^*.

Homalite obeys the maximum principal stress criterion for brittle fracture, then a tensile crack would initiate at a point $\eta_1 = -L^*$ on the upper cohesive surface, where

$$\sigma_1(\eta_1 = -L^*, \eta_2 \rightarrow 0^+) = \sigma_u^H; \tag{54}$$

σ_u^H is the ultimate tensile strength of Homalite, which is $\sim$35 MPa. Note that the shear strength of the crack plane $\tau_o \approx 14$ MPa. For $\beta^* > -1$, σ_1 in some region of the upper cohesive surface attains a value higher than σ_u^H for all intersonic speeds (except for speeds close to β and α), and hence a secondary tensile crack is always initiated. However, for $\beta^* < -1$, the condition is not satisfied for most of the intersonic regime. The position, $\eta_1 = -L^*$, where a tensile crack is initiated, is a strong function of crack speed and β^*. For example, for $\beta^* = -0.4$, the tensile crack would initiate at $L^* \approx 0.95L$ for $v = \sqrt{2}\,\beta$. Figure 16b shows the variation of θ^*, the angle of inclination of the principal plane (see Figure 4b) along the upper cohesive surface. Having determined the position along the upper cohesive surface where a tensile crack is likely to initiate, we can also determine the angle θ^* made by this tensile crack with the vertical from Figure 16b. As mentioned before (see Figure 4b), the angle of inclination (to the vertical) of these tensile cracks in our experiments ranged from 8° to 13°. Two dotted lines are drawn in Figure 16b to indicate the position on the cohesive surface where these cracks might have originated for a crack speed of $\sqrt{2}\,\beta$. Two dotted lines are also drawn in Figure 16a to indicate the magnitude of the maximum principal tensile stress along the secondary crack path in this region, which is close compared to the experimentally measured tensile strength of Homalite (see section 2). Hence the use of the maximum principal stress criterion to predict the origin of these secondary cracks appears to be reasonable.

[50] For $\beta^* = -0.4$ and $v = \sqrt{2}\,\beta$ the angle of inclination $\theta^* \approx 11.2°$. For $\beta^* = 0$ the angle of inclination θ^* of the secondary cracks is identical at all intersonic speeds, being equal to $\sim$21.8°. However, for $\beta^* < 0$, θ^* is always <21.8° and is also a weak function of crack speed. To determine the value of β^* in our laboratory specimens, a plot is made of θ^* versus β^* for different intersonic speeds, as shown in Figure 17. As seen, decreasing β^* reduces the angle of inclination of the secondary cracks and the experimentally observed inclination of $\sim$11° is achieved at $\beta^* \approx -0.4$ for $v = \sqrt{2}\,\beta$. However, at this β^* the angle of inclination varies with the intersonic speed, from $\sim$8° to 14.5°. This variation is close to the variation in measured angle of inclination of the secondary tensile cracks in our experiments. Hence $\beta^* = -0.4$ is a reasonable estimate for the velocity weakening parameter in the zone of nonuniform frictional sliding near an intersonically propagating mode II shear crack in our laboratory specimens. The model predictions are in good agreement with the experimental observations; the orientation of the secondary cracks as predicted is very close, irrespective of the intersonic crack speed, and moreover, its magnitude is also the same as that observed experimentally.

7. Critical Crack Tip Sliding Displacement Criterion

[51] Now we implement the second part of our cohesive law; that is, we introduce a propagation criterion for dynamic mode II crack growth, which states that sustained dynamic mode II crack growth at any sub-Rayleigh or intersonic speed occurs under a constant crack tip sliding displacement (see Figure 7b):

$$\delta_t = u_1(\eta_1 = -L, \eta_2 \rightarrow 0^+) - u_1(\eta_1 = -L, \eta_2 \rightarrow 0^-) = \delta_t^c, \tag{55}$$

where δ_t^c is the critical crack tip sliding displacement or the breakdown slip, a material/specimen specific parameter. In our case, it should depend on the properties of the Homalite-Homalite bond and also strongly on the conditions at the surface of sliding: the nature of bonded surfaces, asperity contacts, whether deformation at asperity

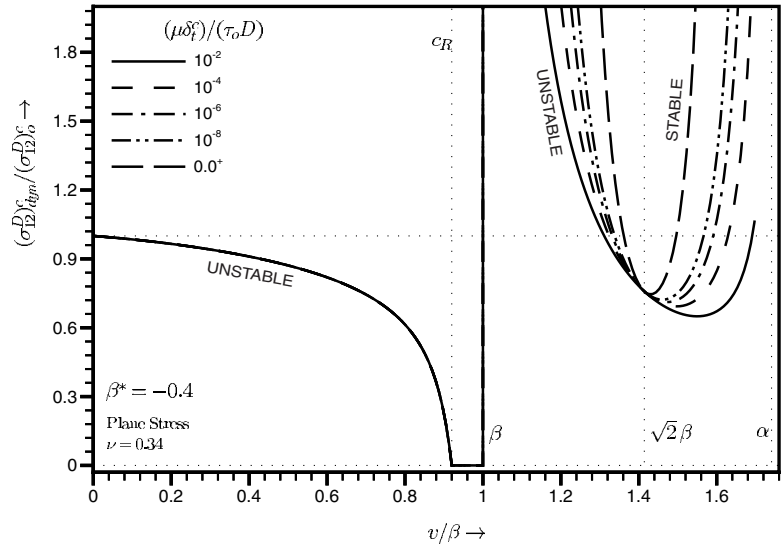

Figure 18. Dynamically propagating mode II crack with a velocity weakening cohesive zone. Stability of crack growth. Dependence of the critical far-field load (required to sustain dynamic crack growth) on crack tip speed v, plotted for $\beta^* = -0.4$ and for different values of the interface strength parameter $(\mu\delta_t^c)/(\tau_o D)$.

contacts occurs by brittle cracking, by plastic flow, or at locally elevated temperature by melting, etc. Such a propagation criterion, which is concerned only with the local state in the vicinity of the crack tip, is more convenient (as compared to a nonlocal criterion like the Griffith's criterion) for modeling the actual physical mechanism of crack growth as well as for application to practical problems using numerical techniques. Also, unlike in the subsonic case, for an intersonic crack the process zone characteristics need to be known to determine the energy flux to the tip region and hence the advantage of employing a small-scale yielding-type approach is lost. Note that with a velocity weakening cohesive zone, the critical crack tip sliding displacement criterion, and the constant critical G criterion (constant fracture energy) are no longer equivalent.

[52] Consider a steadily propagating dynamic mode II crack with a velocity weakening cohesive zone. The crack speed is either subsonic or intersonic ($0 < v < \alpha$). The crack tip sliding displacement, δ_t can be obtained by integrating equation (39) along the cohesive surface. For a shear strength of the crack plane τ_o, a far-field load σ_{12}^D and weakening parameter β^*, the crack tip sliding displacement δ_t is given by

$$\delta_t/\delta_t^o = \begin{cases} \dfrac{2\gamma}{\beta^*}\dfrac{(\alpha_l^2-\alpha_s^2)}{(v^3/\beta^3)}\left[\dfrac{\Gamma(\gamma+1/2)}{\Gamma(\gamma+1)}\right]^2 & 0 \le v < c_R, \\ \dfrac{4\lambda}{\pi\beta^*(1-q)}\dfrac{(\alpha_l^2+\hat{\alpha}_s^2)}{(v^3/\beta^3)}\left(\dfrac{q\pi}{\sin q\pi}\right)^{1/q}\left(\dfrac{\sigma_{12}^D}{\tau_o}\right)^{1/q-2} & \\ \cdot\left[\dfrac{\Gamma(\lambda-q+1)}{\Gamma(1-q)\Gamma(1+\lambda)}\right]^{1/q} & \beta < v < \alpha, \end{cases} \tag{56}$$

where δ_t^o is the crack tip sliding displacement associated with a quasi-statically growing mode II crack under a far-field load σ_{12}^D and shear strength of the crack plane τ_o:

$$\delta_t^o = \frac{\pi(\kappa+1)}{4}\frac{\tau_o}{\mu}\left(\frac{\sigma_{12}^D}{\tau_o}\right)^2 D. \tag{57}$$

The critical crack tip sliding displacement criterion (55) states that $\delta_t = \delta_t^o = \delta_t^c$. Hence equation (56) gives a relationship between the critical values (required to satisfy the criterion) of σ_{12}^D, v, β^*, and τ_o.

[53] Figure 18 shows the variation of the critical far-field load $(\sigma_{12}^D)_{\rm dyn}^c$ (required to satisfy the critical crack tip sliding displacement criterion equation (55)) with crack speed for different values of τ_o at a fixed $\beta^* = -0.4$. Similarly, Figure 19 shows the variation of $(\sigma_{12}^D)_{\rm dyn}^c$ with crack speed for different β^* at a fixed τ_o. The ratio $(\sigma_{12}^D)_{\rm dyn}^c/(\sigma_{12}^D)_o^c$ is given by

$$\frac{(\sigma_{12}^D)_{\rm dyn}^c}{(\sigma_{12}^D)_o^c} = \begin{cases} \sqrt{\left[\dfrac{1}{2}\dfrac{\beta^*}{\gamma}\dfrac{v^3/\beta^3}{\alpha_l^2-\alpha_s^2}\right]}\dfrac{\Gamma(\gamma+1)}{\Gamma(\gamma+1/2)} & 0 \le v < c_R, \\ \left(\dfrac{\mu\delta_t^c}{D\tau_o}\right)^{q-1/2}\left[\dfrac{\beta^*}{2\lambda}\dfrac{v}{\beta}(1-q)\right]^q\sqrt{\left[\dfrac{\pi}{2}\dfrac{1+\hat{\alpha}_s^2}{\alpha_l^2+\hat{\alpha}_s^2}\right]} & \\ \cdot\left(\dfrac{\sin q\pi}{q\pi}\right)\dfrac{\Gamma(1-q)\Gamma(1+\lambda)}{\Gamma(\lambda-q+1)} & \beta < v < \alpha, \end{cases} \tag{58}$$

where the critical far-field load required for quasi-static crack propagation, $(\sigma_{12}^D)_o^c$ is given by

$$(\sigma_{12}^D)_o^c = \tau_o\sqrt{\frac{4}{(\kappa+1)\pi}\frac{\mu\delta_t^c}{D\tau_o}}. \tag{59}$$

[54] As seen from Figures 18 and 19, for a sub-Rayleigh crack, the far-field load required to sustain a small acceleration in crack speed is lower compared to its previous value (decreases with crack speed). This situation may be interpreted as an instability, and it can be expected that a sub-Rayleigh mode II crack would accelerate rapidly to c_R. This is probably the reason why no subsonic crack speeds were observed for mode II shear cracks propagating along a weak plane in Homalite (see Figure 3). Even if the shear crack initiating from the notch initially propagated at sub-

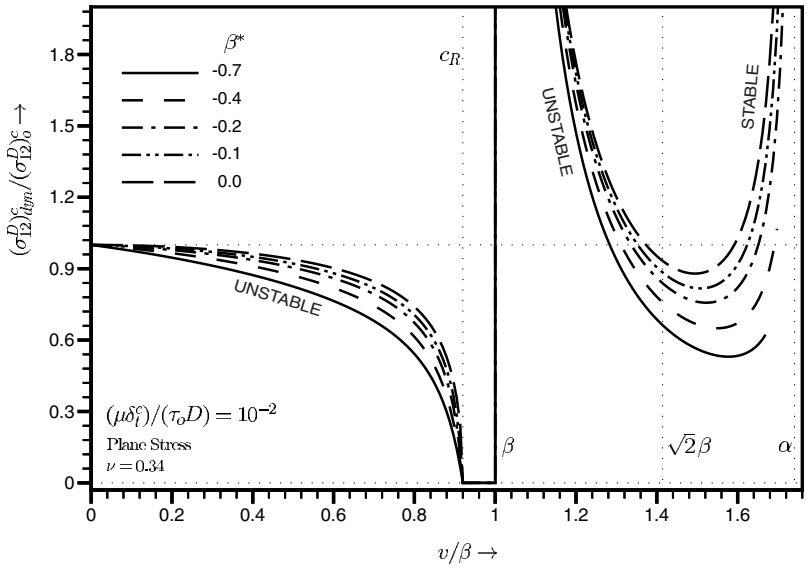

Figure 19. Dynamically propagating mode II crack with a velocity weakening cohesive zone. Stability of crack growth. Dependence of the critical far-field load (required to sustain dynamic crack growth) on crack tip speed v, plotted for $(\mu\delta_t^c)/(\tau_o D) = 10^{-2}$ and for different values of the weakening parameter β^*.

Rayleigh speeds, it would immediately accelerate to c_R and beyond. For sub-Rayleigh crack speeds the critical far-field load $(\sigma_{12}^D)_{\text{dyn}}^c$ is independent of τ_o, whereas lower β^* tends to amplify the instability (see Figure 19). By the same interpretation, for an intersonic crack, there is an initially unstable speed regime followed by a stable speed regime. For intersonic speeds, $(\sigma_{12}^D)_{\text{dyn}}^c/(\sigma_{12}^D)_o^c$ is also a function of τ_o through the material parameter $(\mu\delta_t^c)/(\tau_o D)$; μ and δ_t^c are material constants, and D is an arbitrary distance ahead of the crack tip at which the singular solution with no cohesive zone dominates. Hence the parameter $(\mu\delta_t^c)/(\tau_o D)$ may be interpreted as a measure of shear strength of the fracture plane. It is seen that the entire speed regime $\beta < v < \sqrt{2}\,\beta$ is unstable and the speed at which intersonic crack propagation becomes stable depends on τ_o and β^*. For $\tau_o \rightarrow 0$; that is, for the case of vanishing shear strength of the fracture plane, almost the entire intersonic regime becomes unstable, indicating that a mode II crack on a weak plane of vanishing strength should propagate at speeds close to α. On the other hand, for $\tau_o \rightarrow \infty$ the singular solution with no cohesive zone is recovered, and the onset of stability occurs at $v = \sqrt{2}\,\beta$. Similar observations that the speed regime $\sqrt{2}\,\beta < v < \alpha$ is stable for intersonic mode II crack growth were made by *Burridge et al.* [1979] and *Freund* [1979]. For more realistic values of the parameter $(\mu\delta_t^c)/(\tau_o D) \approx 10^{-2} - 10^{-3}$ and $\beta^* = -0.4$, the critical load required to sustain intersonic crack propagation is a minimum around 1.5β. This explains the observed experimental behavior of crack speed, where the intersonic mode II crack was found to accelerate to speeds close to α and then as the loading pulse was cut off, settled down to a stable propagation speed slightly above $\sqrt{2}\,\beta$. Such a crack speed behavior was also observed by *Needleman* [1999] in his numerical simulations of mode II crack growth along a weak plane. A portion of rupture front during the 1999 Turkey earthquake was also found to propagate at $\sqrt{2}c_s$ [*Bouchon et al.*, 2001].

[55] Here, it must be understood that stability results obtained for a steadily moving semi-infinite crack may be significantly different from those for cracks with more realistic geometries such as the one for an expanding finite crack. This is because one mechanism tending to produce instability in a spreading finite crack, namely, the increase in crack length, is lacking in the case of a steadily moving semi-infinite crack. Thus, if a certain velocity regime is found to unstable for a steadily moving semi-infinite crack, then there is even more reason to suppose that such a regime would also be unstable for an expanding finite crack in a prestressed medium. This is probably the reason why *Broberg* [1994, 1995] found that for a symmetrically expanding mode II crack under uniform remote shear loading, the entire intersonic regime is unstable and that such a crack would accelerate all the way up to α. *Burridge et al.* [1979] also argued that instability is more pronounced in the case of finite cracks undergoing transient crack growth.

[56] The critical cohesive zone length or the cohesive zone size required for sustained mode II crack growth according to the propagation criterion equation (55) is given by

$$\frac{L_{\text{dyn}}^c}{L_o^c} = \begin{cases} \dfrac{1}{2\pi}\dfrac{\beta^*}{\gamma}\dfrac{v}{\beta}\dfrac{1-\alpha_s^2}{\alpha_l^2-\alpha_s^2} & 0 \le v < c_R, \\ \dfrac{1-q}{\pi}\dfrac{\beta^*}{\lambda}\dfrac{v}{\beta}\dfrac{1+\hat{\alpha}_s^2}{\alpha_l^2+\hat{\alpha}_s^2} & \beta < v < \alpha, \end{cases} \tag{60}$$

where the critical cohesive zone length for quasi-static mode II crack propagation L_o^c is given by

$$L_o^c = \frac{\pi}{\kappa+1}\frac{\mu\delta_t^c}{\tau_o}. \tag{61}$$

Hence at any sub-Rayleigh or intersonic crack speed the critical cohesive zone length is directly proportional to the breakdown slip δ_t^c and is inversely proportional to the crack

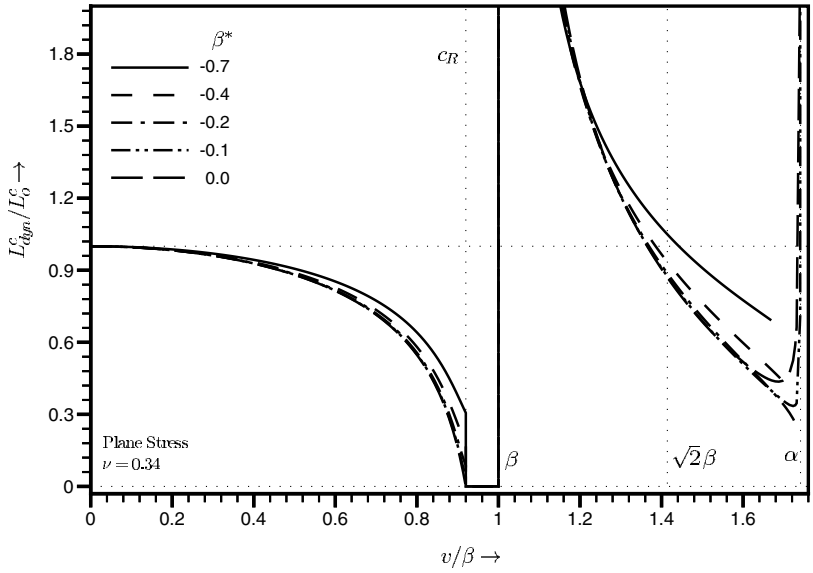

Figure 20. Dynamically propagating mode II crack with a velocity weakening cohesive zone. Variation of the critical cohesive zone length (required to sustain dynamic crack growth) with crack tip speed v, plotted for different values of the weakening parameter β^*.

plane shear strength τ_o. Figure 20 shows the variation of the critical cohesive zone length $L^c_{\rm dyn}/L^c_o$ with crack speed for different values of the rate parameter β^*. The critical cohesive zone size for sub-Rayleigh speeds was found to decrease monotonically up to c_R. It vanishes at c_R in the case of a Dugdale-type cohesive zone ($\beta^* = 0$), whereas it attains a finite value equal to $2|\beta^*|c_R/[\pi(1+\nu)\beta]$ at c_R for any $\beta^* < 0$. In a numerical simulation of a symmetrically expanding mode II crack under the action of remote uniform shear stresses, *Andrews* [1976] found that the cohesive zone size decreases continuously with crack speed in the sub-Rayleigh regime attaining its minimum value at c_R. Such a behavior was also observed in the numerical simulations of *Geubelle and Kubair* [2001]. For intersonic speeds the critical cohesive zone size is unbounded at β and α but remains finite and positive over the rest of the intersonic regime. Such an observation was used by *Yu and Suo* [2000] to justify the admissibility of mode II intersonic crack growth. The critical cohesive zone length is found to be rather insensitive to the rate parameter β^*.

[57] If the propagation of dynamic mode II cracks (with a velocity weakening cohesive zone) is governed by the critical crack tip sliding displacement criterion given in equation (55), then the critical dynamic energy release rate (dissipated fracture energy) is given by

$$\frac{G^c_{\rm dyn}}{G^c_o} = \begin{cases} \dfrac{g(\gamma)}{2\gamma} = \dfrac{\beta^*}{\gamma}\dfrac{v^3}{\beta^3}\dfrac{\alpha_s}{R(v)}\left[\dfrac{\Gamma(\gamma+1)}{\Gamma(\gamma+1/2)}\right]^2 & 0 \le v < c_R, \\ \dfrac{1-q}{\lambda} g^*(\lambda, q) & \beta < v < \alpha, \end{cases} \tag{62}$$

where G^c_o, the critical energy release rate for quasi-static crack propagation is given by

$$G^c_o = \tau_o \delta^c_t. \tag{63}$$

$g(\gamma)$ and $g^*(\lambda, q)$ are given in equation (50). Hence the material/specimen-dependent "fracture energy versus crack speed" curve is strongly influenced by the rate parameter β^*, whereas any variations in the crack plane shear strength τ_o or the critical crack tip sliding displacement δ^c_t merely shift the curve along the "energy" axis.

[58] Figure 21 shows the variation of the dissipated fracture energy (required for sustained mode II crack growth) with crack speed for different values of the weakening parameter β^*. For sub-Rayleigh crack speeds it is found that a velocity weakening cohesive zone ($\beta^* < 0$) dissipates less energy with increasing crack speed and a rate-independent cohesive zone ($\beta^* = 0$) dissipates the same amount of energy irrespective of crack speed. As $v \rightarrow c_R$, the energy dissipated in the cohesive zone vanishes for $\beta^* < 0$. This indicates that sustained mode II crack growth at high sub-Rayleigh crack speeds is more likely with a velocity weakening cohesive zone. Fracture energy required for sustained mode II crack growth at β and α is the same as that for a quasi-static mode II crack. However, for all other intersonic speeds the energy dissipated is lower for $\beta^* < 0$ and remains unchanged for $\beta^* = 0$. The importance of the curious speed of $\sqrt{2}\,\beta$ (vis-a-vis energy dissipated in the tip region) with regard to Freund's singular crack model is diminished.

8. Isochromatic Fringe Patterns

[59] Before comparing the isochromatic fringe patterns predicted by the model with those recorded experimentally, we first estimate the various model parameters and other quantities of interest. As mentioned in section 6, the best estimate for β^* is ~ -0.4. The shear strength of the crack plane τ_o is $\sim$14 MPa (measured). From Figure 6 we estimate the cohesive zone length to be around 2–3 mm ($\sim$2.8 mm at $v = \sqrt{2}\,\beta$). Thus from equations (60) and (61) we compute the critical crack tip sliding displacement (or breakdown slip), δ^c_t to be $\sim$21 μm. Then from equation (62) we obtain the dissipated fracture energy to be <300 J m^{-2} at any sub-Rayleigh or intersonic crack speed. We can also estimate the dynamic fracture toughness, $(K^{*d}_{II})^c_{\rm dyn}$ to be $\sim$1.2 MPa $\sqrt{\rm m}$ (at $v = \sqrt{2}\,\beta$). Later on, we will argue that

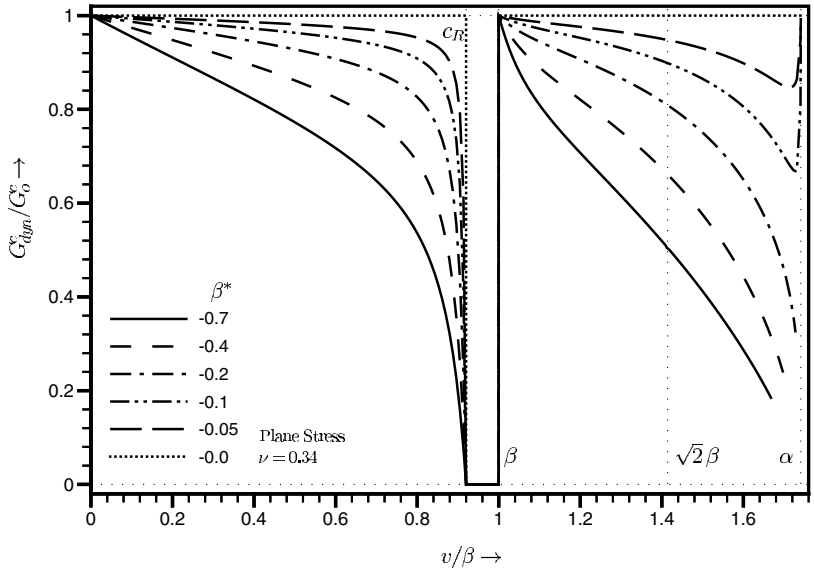

Figure 21. Dynamically propagating mode II crack with a velocity weakening cohesive zone. Variation of the fracture energy (required to sustain dynamic crack growth) with crack tip speed v, plotted for different values of the weakening parameter β^*.

the distance D at which Freund's singular solution dominates is of the order 20–25 mm. For $(K^{*d}_{II})^c_{\rm dyn} \approx 1.2$ MPa $\sqrt{\rm m}$ at $D \approx 25$ mm, the far-field crack plane shear stress, $(\sigma^D_{12})^c_{\rm dyn}$ is ~3 MPa. Hence a measure of the stress drop due to shear rupture in our specimens is ~30 bars. Earlier, we had also mentioned that slip rates in our experiments are of the order of 10 m s^{-1}. As a comparison, for typical crustal earthquakes, slip rates can range from 1 to 10 m s^{-1}, dynamic stress drop can vary from 10^1 to 10^2 bars, total slip (or breakdown slip) is of the order of 1–10 m, rupture speeds can vary from high sub-Rayleigh to 1.4β and fracture energy is of the order $1–10^6$ J m^{-2} [*Rice*, 1980; *Dmowska and Rice*, 1986; *Scholz*, 1990; *Heaton*, 1990; *Bouchon et al.*, 2000; *Ben-Zion*, 2001; *Beroza and Spudich*, 1988].

[60] The near-tip stress field for a steadily propagating sub-Rayleigh or intersonic mode II crack with a velocity weakening cohesive zone is given in Appendix B. From this field, we can construct isochromatic fringe patterns and compare them with those recorded experimentally, so as to check the validity of the assumed cohesive crack model. Under generalized plane stress assumption and within the region of dominance of the near-tip field, the isochromatic fringe order n at any point is given by (see equation (1))

$$n(\eta_1, \eta_2) = \frac{h}{F_\sigma}\sqrt{(\sigma_{11} - \sigma_{22})^2 + 4\sigma^2_{12}}. \qquad (64)$$

where h is the specimen thickness and F_σ is the material fringe constant. F_σ for Homalite is 22.6 KN m^{-1} and the specimen thickness h was chosen to be 4.76 mm (same as in the experiments). The shear crack is assumed to obey a critical crack tip sliding displacement criterion, with $\delta^c_t \approx$ 21 μm. It is also assumed that $\beta^* = -0.4$ and $\mu/\tau_o = 136$, approximating the situation in our experiments.

[61] Figure 22 shows the theoretically predicted isochromatic fringe pattern around a shear crack with a velocity weakening cohesive zone at two different sub-Rayleigh speeds: 0.01β (Figure 22a) and 0.85β (Figure 22b). Similarly, Figure 23 shows the theoretically predicted isochromatic fringe pattern around a shear crack with a velocity weakening cohesive zone at two different intersonic speeds: 1.2β (Figure 23a) and 1.6β (Figure 23b). The field of view shown has a 50 mm diameter, and the front end of the cohesive zone is located on the horizontal diameter ~35 mm from the left edge of the field of view. A horizontal dark line is drawn to indicate the position of the crack faces. A magnified view of the region close to the tip (identified by a rectangle of size 10 mm × 10 mm) is shown as an inset to the right of each pattern. The cohesive zone length was found to be 3 mm at $v = 0.01\beta$, 1.36 mm at $v = 0.85\beta$, 5 mm at $v = 1.2\beta$, and 1.79 mm at $v = 1.6\beta$.

[62] From Figure 22a we see that for a quasi-statically growing mode II crack the isochromatic fringe pattern exhibits a characteristic two-lobed pattern. However as the crack speed approaches c_R (Figure 22b), the shape of the pattern changes dramatically from two lobes to a three-lobed pattern. The cohesive zone size drops as expected (see Figure 20); however, the intensity of the stress field around the crack tip increases substantially (especially off the crack plane). Interestingly, this happens even with a substantial reduction in the "remote" crack plane shear stress (see Figure 19). At $v = 0.85\beta$ the cohesive zone size is small relative to the field of view size of 50 mm, and the isochromatic fringe pattern does not differ markedly from that for a singular solution with no cohesive zone. For the intersonic case we see that the presence of a cohesive zone gives a finite width to the Mach waves emanating from the tip region. For $v = 1.2\beta$ (Figure 23a) the cohesive zone size is large (~5 mm), and the fringe pattern is distinctly different in the three regions: ahead of the Mach waves, within the Mach waves, and behind the Mach waves. For $v = 1.6\beta$ (Figure 23b) the cohesive zone length drops as expected (see Figure 20), and the shape of the fringes behind the Mach waves changes substantially.

[63] Figure 24 compares an experimentally recorded isochromatic fringe pattern to that predicted by the velocity

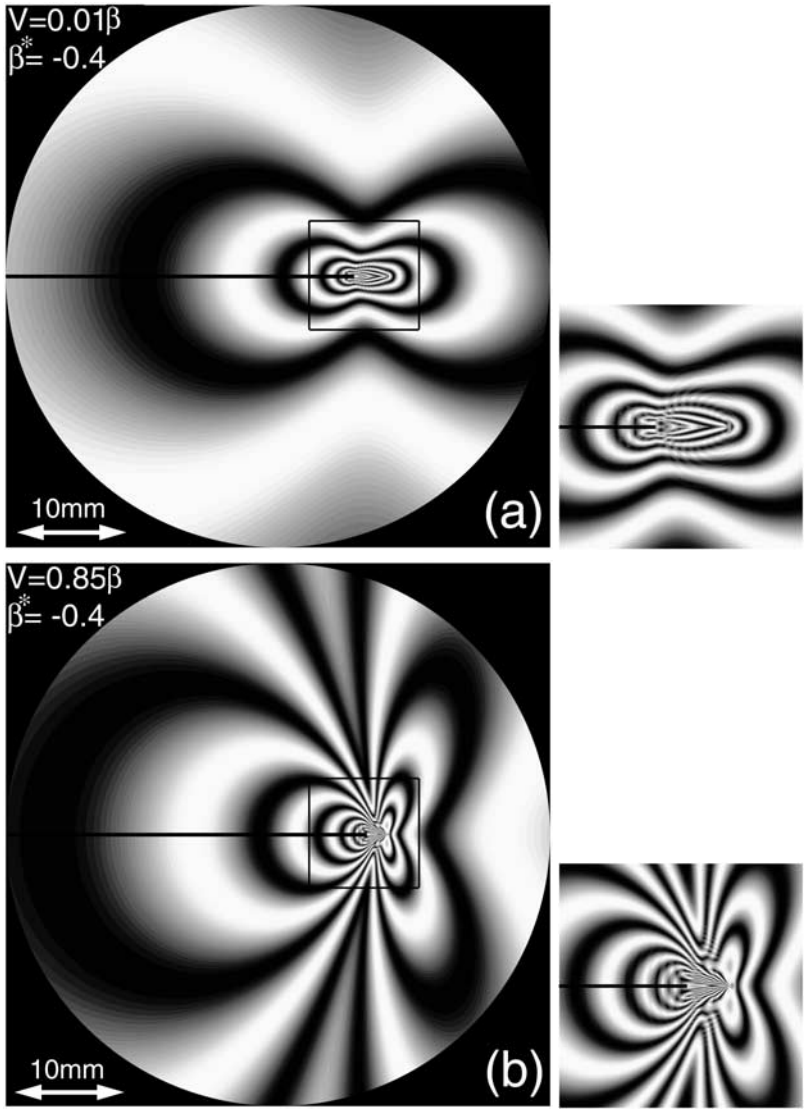

Figure 22. Isochromatic fringe pattern around a propagating subsonic mode II crack with a velocity weakening cohesive zone. The propagating crack obeys a critical crack tip sliding displacement criterion with $\delta_t^c \approx 21$ μm, $\beta^* = -0.4$, and $\mu/\tau_o = 136$. A magnified view of the region around the crack tip (enclosed in the rectangle) is shown on the right. (a) $v/\beta = 0.01$ and $L^c_{\mathrm{dyn}} = 3$ mm. (b) $v/\beta = 0.85$ and $L^c_{\mathrm{dyn}} = 1.36$ mm.

weakening cohesive zone model with $\beta^* = -0.4$. The crack tip speed in both cases was 1.45β. A best fit shows that the intensity of the far-field applied loads, $K_{II}^{*d} \approx 1.04$ MPa m^q. We see that the patterns are similar in a small region close to the crack tip. The cohesive zone solution also introduces some structure across the Mach wave by smearing out the stress jump and eliminating the singularities. Also, the fringe pattern within the finite width of the Mach waves seems to be qualitatively similar. The range of dominance of the current solution seems to be of the order of ~20 mm. Hence features like the ''closed loops'' within the experimental Mach waves (at distances >20 mm), which arise from transient phenomenon, are not captured by the simplified steady state model. The steady state nature of the current solution cannot capture features like the finite length of the Mach waves, transient effects due to changing crack speed, the loading waves still present in the tip vicinity, etc. Also, the distortion of the near-tip fields due to secondary tensile cracks behind the tip is not captured by the current model. However, the model eliminates many pathologies associated with the Freund's singular solution. It eliminates the unphysical singular stresses at the tip as well as along the Mach waves, allows for finite energy flux into the tip at all intersonic speeds, gives finite width and structure to the Mach waves, provides information regarding the processes occurring in the nonlinear zone surrounding the tip, and finally also predicts the orientation of the secondary tensile cracks and explains the reason for they being almost parallel to each other.

9. Discussion

[64] Owing to the importance of the mechanics of dynamic shear crack growth in modeling earthquake source processes, a few comments are in order regarding shear

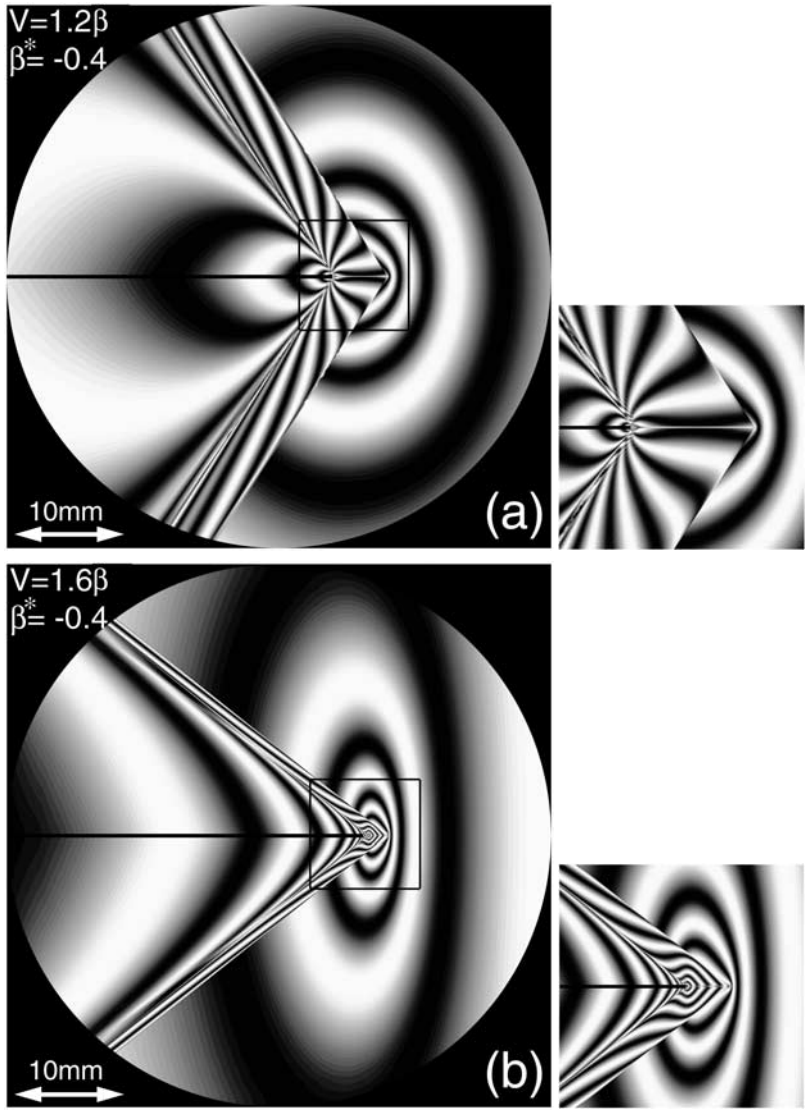

Figure 23. Isochromatic fringe pattern around a propagating intersonic mode II crack with a velocity weakening cohesive zone. The propagating crack obeys a critical crack tip sliding displacement criterion with $\delta_t^c \approx 21$ μm, $\beta^* = -0.4$, and $\mu/\tau_o = 136$. A magnified view of the region around the crack tip (enclosed in the rectangle) is shown on the right. (a) $v/\beta = 1.2$ and $L_{\text{dyn}}^c = 5$ mm. (b) $v/\beta = 1.6$ and $L_{\text{dyn}}^c = 1.79$ mm.

rupture propagation on homogeneous velocity weakening faults. Real earthquake rupture fronts are three-dimensional in nature, and hence the rupture propagation characteristics along the front must be affected by the local ''mode mix'' apart from other factors. However, the current study focuses exclusively on 2-D in-plane shear rupture, and hence the results obtained above (especially those dealing with rupture at intersonic speeds) are of significance mostly along portions of rupture front where the deformation is predominantly mode II. *Heaton* [1990] studied seismic records of several earthquakes and found that the duration of slip at any point on the rupture plane was an order of magnitude smaller than the total duration of rupture propagation. If the rupture propagation was akin to that of an expanding shear crack, both these durations must be of the same order. To resolve the apparent contradiction, he concluded that shear rupture during earthquakes propagates more like a self-healing slip pulse rather than an expanding shear crack. He hypothesized that dynamic velocity weakening friction acting on the fault surfaces may cause the fault to heal itself shortly after the passage of the rupture front, thus causing the rupture to propagate in a self-healing slip pulse like manner. The slip rate diminishes rapidly behind the rupture front, and if the sliding friction acting on the crack faces is velocity weakening, frictional resistance increases substantially a finite distance behind the rupture front, causing the crack faces to lock. Thus a self-healing slip pulse results. Such self-healing slip pulses are unlikely to occur with the current configuration of our laboratory experiments, as a key ingredient, the far-field uniform compressive normal stress (acting on the crack faces), is absent in our experimental setup. This is unlike the crustal faults, a few kilometers beneath the Earth's surface, which are always acted upon by large hydrostatic compressive stresses. The conditions governing the propagation of an earthquake rupture as a self-healing pulse instead of as an extending shear crack were carefully

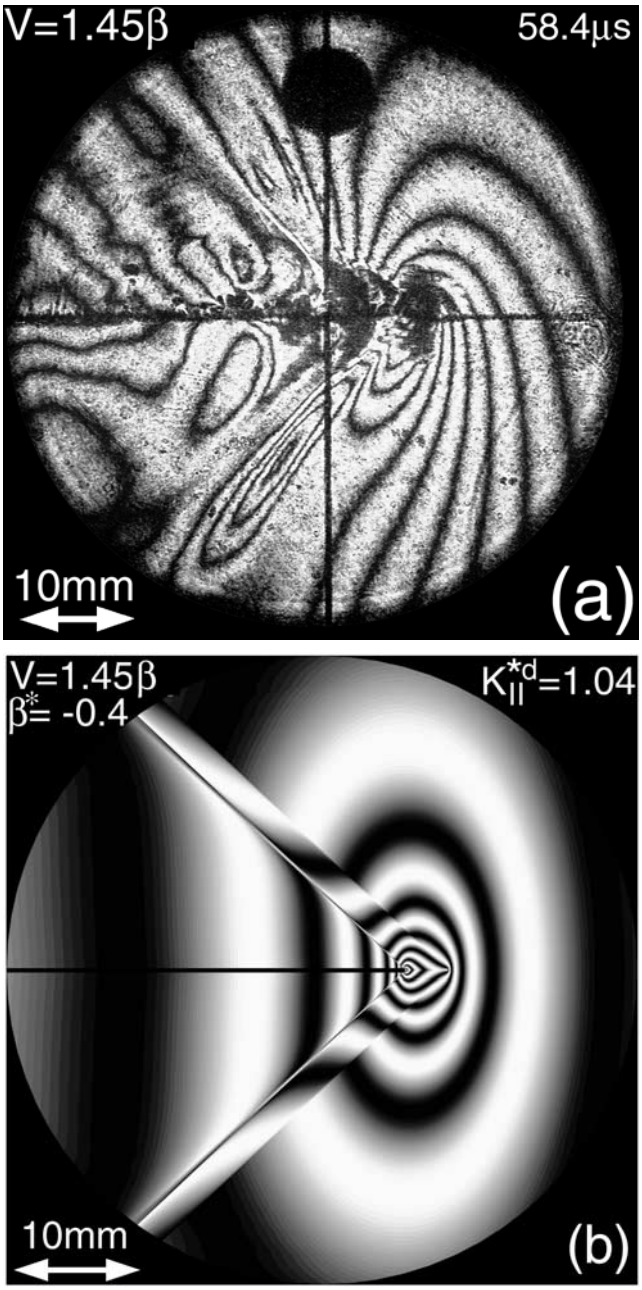

Figure 24. Isochromatic fringe pattern around a propagating intersonic crack along a weak plane in Homalite-100. (a) Experimental observation of the isochromatic fringe pattern around the crack tip with the crack tip speed $v/\beta \approx 1.45$. Note the finite width of the Mach waves. (b) Theoretical prediction based on the velocity weakening cohesive zone model with $\beta^* = -0.4$. The propagating crack is assumed to obey a critical crack tip sliding displacement criterion with $\delta_t^c \approx 30$ μm and $\mu/\tau_o = 136$. Also $v/\beta = 1.45$ and $L^c_{\text{dyn}} = 3.4$ mm.

examined by a number of researchers [*Weertman*, 1980; *Heaton*, 1990; *Cochard and Madariaga*, 1994; *Perrin et al.*, 1995; *Beeler and Tullis*, 1996; *Zheng and Rice*, 1998]. Apart from dynamic velocity weakening friction, other mechanisms like the presence of heterogeneities on the fault plane [*Day*, 1982; *Johnson*, 1990] as well as differing elastic properties across the fault plane [*Andrews and Ben-Zion* 1997; *Harris and Day*, 1997; *Ranjith and Rice*, 2000; *Adams*, 2001; *Cochard and Rice*, 2000; *Ben-Zion*, 2001] were also found to result in the propagation of an earthquake rupture as a self-healing pulse. However, it may be noted that given the heterogeneity of earthquake rupture, risetimes need not always be unreasonably short as expected from a self-healing pulse type rupture propagation [*Beroza and Mikumo*, 1996; *Quin*, 1990].

[65] Unlike our laboratory specimens, where nonuniform sliding friction acts only in a small zone near the crack tip, on a homogeneous fault (containing rocks with similar elastic properties on either side of the rupture plane), sliding friction acts over the entire crack faces. *Perrin et al.* [1995] showed that self-healing slip pulse solutions do not exist for pure velocity weakening friction laws, i.e., for laws of the type considered in this paper. They showed that sliding surfaces which follow both rate- and state-dependent friction laws allowing for restrengthening under stationary contact can sustain self-healing slip pulses. *Zheng and Rice* [1998] introduced a dimensionless measure of the rate of velocity weakening T given by

$$T = \frac{1}{(\mu/2\beta)} \frac{-d\tau(\dot{\delta})}{d\dot{\delta}}, \tag{65}$$

which is one of the major parameters governing the transition of an initiated shear rupture into a self-healing pulse. With a velocity weakening law of the type equation (29) we have $T = -\beta^*$, and from our estimate of β^* from section 6 we have $T = 0.4$. In their two-dimensional antiplane simulations, *Zheng and Rice* [1998] found that an extending shear rupture transitions into a self-healing pulse for $T > 0.5$. The experimentally measured value of T, though not directly comparable, is close to this transition cutoff. However, if the transition value of T is similar, it is plausible that in the presence of a far-field compressive normal stress acting on the weak plane, self-healing pulses may be obtained even in our laboratory specimens.

Appendix A: Solution to the Cauchy-Type Singular Integral Equation

[66] The solution procedure for the integral equation (31) is shown here only for the intersonic case. The procedure for the subsonic case is similar and is omitted.

$$\hat{f}(\eta_1)\left\{1 + \beta^* \frac{v^3}{\beta^3} \frac{\hat{\alpha}_s}{R_q} \cos q\pi\right\} - \left\{\beta^* \frac{v^3}{\beta^3} \frac{\hat{\alpha}_s}{R_q} \sin q\pi\right\}$$

$$\cdot \frac{1}{\pi} \text{pv} \int_{-L}^{0} \frac{\hat{f}(\xi)}{(\xi + |\eta_1|)} d\xi = \frac{1}{|\eta_1|^{1-q}} \qquad \beta < v < \alpha, \tag{A1}$$

where

$$\hat{f}(\eta_1) = \frac{\tau(\eta_1/L)}{\tau_o |\eta_1|^{1-q}} \qquad \beta < v < \alpha. \tag{A2}$$

Define a Cauchy-type integral,

$$\phi(z) = \frac{1}{2\pi i} \int_{-L}^{0} \frac{\hat{f}(\xi)}{\xi - z} d\xi. \tag{A3}$$

If we assume that $\hat{f}(\eta_1)$ satisfies the Hölder condition, then by Plemelj formulae,

$$(A - iB)\phi^+(\eta_1) - (A + iB)\phi^-(\eta_1) = \frac{1}{|\eta_1|^{1-q}}, \tag{A4}$$

where

$$A = 1 + \beta^* \frac{v^3}{\beta^3} \frac{\hat{\alpha}_s}{R_q} \cos\, q\pi, \tag{A5}$$

$$B = \beta^* \frac{v^3}{\beta^3} \frac{\hat{\alpha}_s}{R_q} \sin\, q\pi. \tag{A6}$$

Equation (A4) can be rewritten as

$$\left(\frac{\phi}{z^\lambda}\right)^+ - \left(\frac{\phi}{z^\lambda}\right)^- = \frac{1}{\sqrt{A^2 + B^2}} \frac{1}{|\eta_1|^{1-q}}, \tag{A7}$$

where

$$\lambda = \frac{1}{\pi} \tan^{-1}\left(\frac{B}{A}\right). \tag{A8}$$

Rearranging equation (A7) as

$$\left[\frac{(z+L)^{\lambda_1}\phi}{z^{\lambda+n}}\right]^+ - \left[\frac{(z+L)^{\lambda_1}\phi}{z^{\lambda+n}}\right]^- = \frac{1}{\sqrt{A^2 + B^2}} \cdot \frac{(\eta_1 + L)^{\lambda_1}}{|\eta_1|^{\lambda+n+1-q}} (-1)^n, \tag{A9}$$

where n, an integer, and λ_1 are to be determined, we obtain a Riemann-Hilbert (R-H) problem.

[67] The general solution of the R-H problem above is given by

$$\frac{(z+L)^{\lambda_1}\phi}{z^{n+\lambda}} = P(z) + \frac{1}{2\pi i} \int_{-L}^{0} \frac{1}{\sqrt{A^2 + B^2}} \frac{(\eta_1 + L)^{\lambda_1} (-1)^n}{|\eta_1|^{\lambda+n+1-q}} \cdot \frac{1}{\eta_1 - z} d\eta_1. \tag{A10}$$

$P(z)$ is an entire function (a polynomial). Ensuring that both sides have the same behavior as $|z| \to \infty$, we obtain $\lambda_1 = \lambda + m$, where m is an integer.

$$\hat{f}(\eta_1) = \phi^+(\eta_1) - \phi^-(\eta_1). \tag{A11}$$

$$\Rightarrow \hat{f}(\eta_1) = \frac{\cos \lambda\pi}{\sqrt{A^2 + B^2}} \frac{1}{|\eta_1|^{1-q}} + \frac{|\eta_1|^{n+\lambda}}{(\eta_1 + L)^{\lambda+m}} \frac{\sin \lambda\pi}{\sqrt{A^2 + B^2}} \cdot \left\{ P(z) \text{ of order } m - 1 - n. + \frac{1}{\pi} \text{pv} \int_{-L}^{0} \frac{(\xi + L)^{\lambda+m}}{|\xi|^{1-q+\lambda+m}} \frac{1}{\xi - \eta_1} d\xi \right\}. \tag{A12}$$

Introducing the boundary condition (see equation (34)),

$$\lim_{\eta_1 \to 0} \hat{f} = \frac{1}{|\eta_1|^{1-q}}, \tag{A13}$$

we obtain $n = 0$. Introducing the second boundary condition (see equation (34)),

$$\left[\lim_{\eta_1 \to -L} \hat{f}\right] (\eta_1 + L)^q |\eta_1|^{1-q} \to 0, \tag{A14}$$

we obtain $m = 0$ and $P(z) = 0$. Thus all the unknown quantities are determined. After some further simplification the cohesive traction distribution is obtained as

$$\frac{\tau(-1 < \eta_1/L \le 0)}{\tau_o} = 1 + \frac{\sin \lambda\pi}{\pi} \frac{(-\eta_1/L)^{1-q+\lambda}}{(1 + \eta_1/L)^\lambda} \cdot \int_0^1 \frac{(1-s)^\lambda}{s^q (1 + s\,\eta_1/L)} ds \qquad \beta < v < \alpha. \tag{A15}$$

By a similar procedure the cohesive traction distribution for subsonic speeds can be obtained.

$$\frac{\tau(-1 < \eta_1/L \le 0)}{\tau_o} = 1 + \frac{\sin \gamma\pi}{\pi} \frac{(-\eta_1/L)^{\gamma+1/2}}{(1 + \eta_1/L)^\gamma} \cdot \int_0^1 \frac{(1-s)^\gamma}{\sqrt{s}(1 + s\,\eta_1/L)} ds \quad 0 \le v < c_R, \tag{A16}$$

where

$$\gamma = \frac{1}{\pi} \tan^{-1}\left\{\beta^* \frac{v^3}{\beta^3} \frac{\alpha_s}{R(v)}\right\} \qquad 0 \le v < c_R. \tag{A17}$$

Appendix B: Near-Tip Stress Fields

[68] The stress field around the tip of a sub-Rayleigh crack with a velocity weakening cohesive zone is given by

$$\frac{\sigma_{11}}{\tau_o} = \frac{2\alpha_s}{\pi R(v)} \left[\left(1 + 2\alpha_l^2 - \alpha_s^2\right) \sqrt{\frac{r_l}{L}} \sin\left(\frac{\theta_l}{2}\right) \cdot \left\{ \int_0^1 \frac{\left[\zeta - \left(\frac{r_l}{L}\right)\right]}{\sqrt{\zeta}\left[\zeta^2 + \left(\frac{r_l}{L}\right)^2 + 2\zeta\left(\frac{r_l}{L}\right)\cos\theta_l\right]} d\zeta + \frac{\sin \gamma\pi}{\pi} \cdot \int_0^1 \left(\frac{\zeta}{1-\zeta}\right)^\gamma \frac{\left[\zeta - \left(\frac{r_l}{L}\right)\right]}{\left[\zeta^2 + \left(\frac{r_l}{L}\right)^2 + 2\zeta\left(\frac{r_l}{L}\right)\cos\,\theta_l\right]} \int_0^1 \frac{(1-s)^\gamma}{\sqrt{s}(1 - s\zeta)} ds\, d\zeta \right\} - \left(1 + \alpha_s^2\right) \sqrt{\frac{r_s}{L}} \sin\left(\frac{\theta_s}{2}\right) \left\{ \int_0^1 \frac{\left[\zeta - \left(\frac{r_s}{L}\right)\right]}{\sqrt{\zeta}\left[\zeta^2 + \left(\frac{r_s}{L}\right)^2 + 2\zeta\left(\frac{r_s}{L}\right)\cos\theta_s\right]} d\zeta + \frac{\sin\gamma\pi}{\pi} \int_0^1 \left(\frac{\zeta}{1-\zeta}\right)^\gamma \frac{\left[\zeta - \left(\frac{r_s}{L}\right)\right]}{\left[\zeta^2 + \left(\frac{r_s}{L}\right)^2 + 2\zeta\left(\frac{r_s}{L}\right)\cos\,\theta_s\right]} \cdot \int_0^1 \frac{(1-s)^\gamma}{\sqrt{s}(1 - s\zeta)} ds\, d\zeta \right\} \right], \tag{B1a}$$

$$\frac{\sigma_{22}}{\tau_o}=\frac{2\alpha_s}{\pi R(v)}\left[-\left(1+\alpha_s^2\right)\sqrt{\frac{r_l}{L}}\sin\left(\frac{\theta_l}{2}\right)\right.$$
$$\cdot\left\{\int_0^1\frac{\left[\zeta-\left(\frac{r_l}{L}\right)\right]}{\sqrt{\zeta}\left[\zeta^2+\left(\frac{r_l}{L}\right)^2+2\zeta\left(\frac{r_l}{L}\right)\cos\theta_l\right]}d\zeta+\frac{\sin\gamma\pi}{\pi}\right.$$
$$\left.\cdot\int_0^1\left(\frac{\zeta}{1-\zeta}\right)^{\gamma}\frac{\left[\zeta-\left(\frac{r_l}{L}\right)\right]}{\left[\zeta^2+\left(\frac{r_l}{L}\right)^2+2\zeta\left(\frac{r_l}{L}\right)\cos\theta_l\right]}\int_0^1\frac{(1-s)^{\gamma}}{\sqrt{s}(1-s\zeta)}ds\,d\zeta\right\}$$
$$+\left(1+\alpha_s^2\right)\sqrt{\frac{r_s}{L}}\sin\left(\frac{\theta_s}{2}\right)\left\{\int_0^1\frac{\left[\zeta-\left(\frac{r_s}{L}\right)\right]}{\sqrt{\zeta}\left[\zeta^2+\left(\frac{r_s}{L}\right)^2+2\zeta\left(\frac{r_s}{L}\right)\cos\theta_s\right]}d\zeta\right.$$
$$+\frac{\sin\gamma\pi}{\pi}\int_0^1\left(\frac{\zeta}{1-\zeta}\right)^{\gamma}\frac{\left[\zeta-\left(\frac{r_s}{L}\right)\right]}{\left[\zeta^2+\left(\frac{r_s}{L}\right)^2+2\zeta\left(\frac{r_s}{L}\right)\cos\theta_s\right]}$$
$$\left.\left.\cdot\int_0^1\frac{(1-s)^{\gamma}}{\sqrt{s}(1-s\zeta)}ds\,d\zeta\right\}\right],\tag{B1b}$$

$$\frac{\sigma_{12}}{\tau_o}=\frac{1}{\pi R(v)}\left[4\alpha_l\alpha_s\sqrt{\frac{r_l}{L}}\cos\left(\frac{\theta_l}{2}\right)\right.$$
$$\cdot\left\{\int_0^1\frac{\left[\zeta+\left(\frac{r_l}{L}\right)\right]}{\sqrt{\zeta}\left[\zeta^2+\left(\frac{r_l}{L}\right)^2+2\zeta\left(\frac{r_l}{L}\right)\cos\theta_l\right]}d\zeta+\frac{\sin\gamma\pi}{\pi}\right.$$
$$\left.\cdot\int_0^1\left(\frac{\zeta}{1-\zeta}\right)^{\gamma}\frac{\left[\zeta+\left(\frac{r_l}{L}\right)\right]}{\left[\zeta^2+\left(\frac{r_l}{L}\right)^2+2\zeta\left(\frac{r_l}{L}\right)\cos\theta_l\right]}\int_0^1\frac{(1-s)^{\gamma}}{\sqrt{s}(1-s\zeta)}ds\,d\zeta\right\}$$
$$-\left(1+\alpha_s^2\right)^2\sqrt{\frac{r_s}{L}}\cos\left(\frac{\theta_s}{2}\right)\left\{\int_0^1\frac{\left[\zeta+\left(\frac{r_s}{L}\right)\right]}{\sqrt{\zeta}\left[\zeta^2+\left(\frac{r_s}{L}\right)^2+2\zeta\left(\frac{r_s}{L}\right)\cos\theta_s\right]}d\zeta\right.$$
$$+\frac{\sin\gamma\pi}{\pi}\int_0^1\left(\frac{\zeta}{1-\zeta}\right)^{\gamma}\frac{\left[\zeta+\left(\frac{r_s}{L}\right)\right]}{\left[\zeta^2+\left(\frac{r_s}{L}\right)^2+2\zeta\left(\frac{r_s}{L}\right)\cos\theta_s\right]}$$
$$\left.\left.\cdot\int_0^1\frac{(1-s)^{\gamma}}{\sqrt{s}(1-s\zeta)}ds\,d\zeta\right\}\right],\tag{B1c}$$

where

$$r_s=\sqrt{\eta_1^2+\alpha_s^2\eta_2^2},\qquad \theta_s=\tan^{-1}\left[\frac{\alpha_s\eta_2}{\eta_1}\right],\tag{B2a}$$

$$r_l=\sqrt{\eta_1^2+\alpha_l^2\eta_2^2},\qquad \theta_l=\tan^{-1}\left[\frac{\alpha_l\eta_2}{\eta_1}\right].\tag{B2b}$$

[69] The stress field around the tip of an intersonic crack with a velocity weakening cohesive zone is given by

$$\frac{\sigma_{11}}{\tau_o}=\frac{\sin q\pi}{2\pi\alpha_l}\left[\left(1+2\alpha_l^2+\hat{\alpha}_s^2\right)\left(\frac{r_l}{L}\right)^{1-q}\right.$$
$$\cdot\left\{\int_0^1\frac{\left[\zeta\sin(1-q)\theta_l-\left(\frac{r_l}{L}\right)\sin q\theta_l\right]}{\zeta^{1-q}\left[\zeta^2+\left(\frac{r_l}{L}\right)^2+2\zeta\left(\frac{r_l}{L}\right)\cos\theta_l\right]}d\zeta+\frac{\sin\lambda\pi}{\pi}\right.$$
$$\left.\cdot\int_0^1\left(\frac{\zeta}{1-\zeta}\right)^{\lambda}\frac{\left[\zeta\sin(1-q)\theta_l-\left(\frac{r_l}{L}\right)\sin q\theta_l\right]}{\left[\zeta^2+\left(\frac{r_l}{L}\right)^2+2\zeta\left(\frac{r_l}{L}\right)\cos\theta_l\right]}\right.$$
$$\left.\cdot\int_0^1\frac{(1-s)^{\lambda}}{s^q(1-s\zeta)}ds\,d\zeta\right\}$$
$$-\left(1-\hat{\alpha}_s^2\right)\sin q\pi\xi^{1-q}\left\{\int_0^1\frac{d\zeta}{\zeta^{1-q}(\zeta-\xi)}+\int_0^1\frac{ds}{s^q(1-s\,\xi)}\right.$$
$$\left.\left.-Q(\xi,\lambda)\int_0^1\frac{(1-s)^{\lambda}}{s^q(1-s\xi)}ds\right\}H(\xi)\right],\tag{B3a}$$

$$\frac{\sigma_{22}}{\tau_o}=\frac{\sin q\pi}{2\pi\alpha_l}\left[-\left(1-\hat{\alpha}_s^2\right)\left(\frac{r_l}{L}\right)^{1-q}\right.$$
$$\cdot\left\{\int_0^1\frac{\left[\zeta\sin(1-q)\theta_l-\left(\frac{r_l}{L}\right)\sin q\theta_l\right]}{\zeta^{1-q}\left[\zeta^2+\left(\frac{r_l}{L}\right)^2+2\zeta\left(\frac{r_l}{L}\right)\cos\theta_l\right]}d\zeta+\frac{\sin\lambda\pi}{\pi}\right.$$
$$\cdot\int_0^1\left(\frac{\zeta}{1-\zeta}\right)^{\lambda}\frac{\left[\zeta\sin(1-q)\theta_l-\left(\frac{r_l}{L}\right)\sin q\theta_l\right]}{\left[\zeta^2+\left(\frac{r_l}{L}\right)^2+2\zeta\left(\frac{r_l}{L}\right)\cos\theta_l\right]}$$
$$\left.\cdot\int_0^1\frac{(1-s)^{\lambda}}{s^q(1-s\zeta)}ds\,d\zeta\right\}$$
$$+\left(1-\hat{\alpha}_s^2\right)\sin q\pi\xi^{1-q}\left\{\int_0^1\frac{d\zeta}{\zeta^{1-q}(\zeta-\xi)}+\int_0^1\frac{ds}{s^q(1-s\xi)}\cdot\right.$$
$$\left.-Q(\xi,\lambda)\int_0^1\frac{(1-s)^{\lambda}}{s^q(1-s\,\xi)}ds\right\}H(\xi)\Bigg],\tag{B3b}$$

$$\frac{\sigma_{12}}{\tau_o}=\frac{\sin q\pi}{\pi}\left[\left(\frac{r_l}{L}\right)\left(\frac{r_l}{L}\right)^{1-q}\right.$$
$$\cdot\left\{\int_0^1\frac{\left[\zeta\cos(1-q)\theta_l+\left(\frac{r_l}{L}\right)\cos q\theta_l\right]}{\zeta^{1-q}\left[\zeta^2+\left(\frac{r_l}{L}\right)^2+2\zeta\left(\frac{r_l}{L}\right)\cos\theta_l\right]}d\zeta\quad+\frac{\sin\lambda\pi}{\pi}\right.$$
$$\cdot\int_0^1\left(\frac{\zeta}{1-\zeta}\right)^{\lambda}\frac{\left[\zeta\cos(1-q)\theta_l+\left(\frac{r_l}{L}\right)\cos q\theta_l\right]}{\left[\zeta^2+\left(\frac{r_l}{L}\right)^2+2\zeta\left(\frac{r_l}{L}\right)\cos\theta_l\right]}$$
$$\left.\cdot\int_0^1\frac{(1-s)^{\lambda}}{s^q(1-s\zeta)}ds\,d\zeta\right\}\quad+\cos q\pi\,\xi^{1-q}$$
$$\cdot\left\{\int_0^1\frac{d\zeta}{\zeta^{1-q}(\zeta-\xi)}+\int_0^1\frac{ds}{s^q(1-s\,\xi)}\right.$$
$$\left.\left.-Q(\xi,\lambda)\int_0^1\frac{(1-s)^{\lambda}}{s^q(1-s\xi)}ds\right\}H(\xi)\right],\tag{B3c}$$

where

$$Q(\xi,\lambda)=\begin{cases}\cos\pi\lambda\left(\frac{\xi}{1-\xi}\right)^{\lambda} & \xi<1,\\ \left(\frac{-\xi}{1-\xi}\right)^{\lambda} & \xi>1,\end{cases}\tag{B4a}$$

$$\xi=\frac{-\eta_1-\hat{\alpha}_s\eta_2}{L}.\tag{B4b}$$

[70] **Acknowledgments.** The authors gratefully acknowledge the support of the National Science Foundation (grants CMS9813100 and CMS9983779) and of the Office of Naval Research (grants N00014-95-

1-0453 and N00014-01-1-0204, Y. D. S. Rajapakse, Project Monitor). Many helpful discussions with J. R. Rice of Harvard University and A. Needleman of Brown University are also acknowledged.

References

Abraham, F. F., and H. J. Gao, How fast can cracks propagate?, *Phys. Rev. Lett.*, *84*, 3113–3116, 2000.

Adams, G. G., An intersonic slip pulse at a frictional interface between dissimilar materials, *J. Appl. Mech.*, *68*, 81–86, 2001.

Andrews, D. J., Rupture velocity of plane strain shear cracks, *J. Geophys. Res.*, *81*, 5679–5687, 1976.

Andrews, D. J., and Y. Ben-Zion, Wrinkle-like slip pulse on a fault between different materials, *J. Geophys. Res.*, *102*, 553–571, 1997.

Archuleta, R. J., A faulting model for the 1979 Imperial Valley earthquake, *J. Geophys. Res.*, *89*, 4559–4585, 1984.

Barenblatt, G. I., The mathematical theory of equilibrium cracks in brittle fracture, *Adv. Appl. Mech.*, *7*, 55–129, 1962.

Beeler, N. M., and T. E. Tullis, Self-healing slip pulses in dynamic rupture models due to velocity-dependent strength, *Bull. Seismol. Soc. Am.*, *86*, 1130–1148, 1996.

Ben-Zion, Y., Dynamic rupture in recent models of earthquake faults, *J. Mech. Phys. Solids*, *49*, 2209–2244, 2001.

Beroza, G. C., and T. Mikumo, Short slip duration in the presence of heterogeneous fault properties, *J. Geophys. Res.*, *101*, 22,449–22,460, 1996.

Beroza, G. C., and P. Spudich, Linearized inversion for fault rupture behavior: Application to the 1984 Morgan Hill, California, earthquake, *J. Geophys. Res.*, *93*, 6275–6296, 1988.

Bouchon, M., N. Toksöz, H. Karabulut, M. P. Bouin, M. Dietrich, M. Aktar, and M. Edie, Seismic imaging of the 1999 Izmit (Turkey) rupture inferred from the near-fault recordings, *Geophys. Res. Lett.*, *27*, 3013–3016, 2000.

Bouchon, M., M. P. Bouin, H. Karabulut, M. N. Toksöz, M. Dietrich, and A. J. Rosakis, How fast is rupture during an eaerthquake? New sights from the 1999 Turkey earthquakes, *Geophys. Res. Lett.*, *28*, 2723–2726, 2001.

Broberg, K. B., On crack paths, *Eng. Fract. Mech.*, *28*, 663–679, 1987.

Broberg, K. B., The near-tip field at high crack velocities, *Int. J. Fract.*, *39*, 1–13, 1989.

Broberg, K. B., Intersonic bilateral slip, *Geophys. J. Int.*, *119*, 706–714, 1994.

Broberg, K. B., Intersonic mode II crack expansion, *Arch. Mech.*, *47*, 859–871, 1995.

Broberg, K. B., How fast can a crack go?, *Mater. Sci.*, *32*, 80–86, 1996.

Broberg, K. B., Intersonic mode II crack acceleration, *Fatigue Fract. Eng. Mater. Struct.*, *22*, 17–24, 1999a.

Broberg, K. B., *Cracks and Fracture*, Academic, San Diego, Calif., 1999b.

Burridge, R., Admissible speeds for plane strain shear cracks with friction but lacking cohesion, *Geophys. J. R. Astron. Soc.*, *35*, 439–455, 1973.

Burridge, R., G. Conn, and L. B. Freund, The stability of a rapid mode II shear crack with finite cohesive traction, *J. Geophys. Res.*, *84*, 2210–2222, 1979.

Cochard, A., and R. Madariaga, Dynamic faulting under rate-dependent friction, *Pure Appl. Geophys.*, *142*, 419–445, 1994.

Cochard, A., and J. R. Rice, Fault rupture between dissimilar materials: Ill-posedness, regularization and slip-pulse response, *J. Geophys. Res.*, *105*, 25,891–25,907, 2000.

Coker, D., and A. J. Rosakis, Experimental observations of intersonic crack growth in asymmetrically loaded unidirectional composite plates, *Philos. Mag.*, *81*, 571–595, 2001.

Cotterell, B., and J. R. Rice, Slightly curved or kinked cracks, *Int. J. Fract.*, *16*, 155–169, 1980.

Curran, D. A., D. A. Shockey, and S. Winkler, Crack propagation at supersonic velocities, II, Theoretical model, *Int. J. Fract. Mech.*, *6*, 271–278, 1970.

Dally, J. W., and W. F. Riley, *Experimental Stress Analysis*, McGraw-Hill, New York, 1991.

Das, S., Application of dynamic shear crack models to the study of the earthquake faulting process, *Int. J. Fract.*, *27*, 263–276, 1985.

Das, S., and K. Aki, A numerical study of two-dimensional spontaneous rupture propagation, *Geophys. J. R. Astron. Soc.*, *50*, 643–668, 1977.

Day, S. M., Three-dimensional simulation of spontaneous rupture: The effect of non-uniform prestress, *Bull. Seismol. Soc. Am.*, *72*, 1881–1902, 1982.

Dmowska, R., and J. R. Rice, Fracture theory and its seismological applications, in *Continuum Theories in Solid Earth Physics*, edited by R. Teisseyre, pp. 187–255, Elsevier Sci., New York, 1986.

Dugdale, D. S., Yielding of steel sheets containing slits, *J. Mech. Phys. Solids*, *8*, 100–104, 1960.

Ellsworth, W. L., and M. Celebi, Near-field displacement time histories of the *M* 7.4 Kocaeli (Izimit), Turkey, earthquake of August 17, 1999, *Eos Trans. AGU*, *80*(46), Fall Meet. Suppl. F648, 1999.

Fineberg, J., and M. Marder, Instability in dynamic fracture, *Phys. Rep.*, *313*, 2–108, 1999.

Freund, L. B., The mechanics of dynamic shear crack propagation, *J. Geophys. Res.*, *84*, 2199–2209, 1979.

Freund, L. B., *Dynamic Fracture Mechanics*, Cambridge Univ. Press, New York, 1990.

Freund, L. B., and Y. J. Lee, Observations on high strain rate crack growth based on a strip yield model, *Int. J. Fract.*, *42*, 261–276, 1990.

Gakhov, F. D., *Boundary Value Problems*, Dover, Mineola, N. Y., 1990.

Gao, H., Y. Huang, P. Gumbsch, and A. J. Rosakis, On radiation-free transonic motion of cracks and dislocations, *J. Mech. Phys. Solids*, *47*, 1941–1961, 1999.

Gao, H., Y. Huang, and F. A. Abraham, Continuum and atomistic studies of intersonic crack propagation, *J. Mech. Phys. Solids*, *49*, 2113–2132, 2001.

Gao, H. J., Surface roughening and branching instabilities in dynamic fracture, *J. Mech. Phys. Solids*, *41*, 457–486, 1993.

Geubelle, P. H., and D. Kubair, Intersonic crack propagation in homogeneous media under shear dominated loading—Numerical analysis, *J. Mech. Phys. Solids*, *49*, 571–587, 2001.

Glennie, E. B., A strain-rate dependent crack model, *J. Mech. Phys. Solids*, *19*, 255–272, 1971a.

Glennie, E. B., The unsteady motion of a rate-dependent crack model, *J. Mech. Phys. Solids*, *19*, 329–338, 1971b.

Harris, R. A., and S. M. Day, Effects of a low-velocity zone on a dynamic rupture, *Bull. Seismol. Soc. Am.*, *87*, 1267–1280, 1997.

Heaton, T. H., Evidence for and implications of self-healing pulses of slip in earthquake rupture, *Phys. Earth Planet. Inter.*, *64*, 1–20, 1990.

Hernandez, B., F. Cotton, and M. Campillo, Contribution of radar interferometry to a two-step inversion of the kinematic process of the 1992 Landers earthquake, *J. Geophys. Res.*, *104*, 13,083–13,099, 1999.

Huang, Y., W. Wang, C. Liu, and A. J. Rosakis, Analysis of intersonic crack growth in unidirectional fiber-reinforced composites, *J. Mech. Phys. Solids*, *47*, 1893–1916, 1999.

Ida, Y., Cohesive force across the tip of a longitudinal-shear crack and Griffith's specific surface energy, *J. Geophys. Res.*, *77*, 3796–3805, 1972.

Johnson, E., On the initiation of unidirectional slip, *Geophys. J. Int.*, *101*, 125–132, 1990.

Johnson, E., Process region changes for rapidly propagating cracks, *Int. J. Fract.*, *55*, 47–63, 1992.

Kilgore, B. D., M. L. Blanpied, and J. H. Dieterich, Velocity dependent friction of granite over a wide range of conditions, *Geophys. Res. Lett.*, *20*, 903–906, 1993.

Lambros, J., and A. J. Rosakis, Shear dominated transonic interfacial crack growth in a bimaterial, 1, Experimental observations, *J. Mech. Phys. Solids*, *43*, 169–188, 1995.

Lee, O. S., and W. G. Knauss, Dynamic crack propagation along a weakly bonded plane in a polymer, *Exp. Mech.*, *29*, 342–345, 1989.

Lee, Y. J., and L. B. Freund, Fracture initiation due to asymmetric impact loading of an edge cracked plate, *J. Appl. Mech.*, *57*, 104–111, 1990.

Melin, S., When does a crack grow under mode II conditions, *Int. J. Fract.*, *30*, 103–114, 1986.

Muskhelishvili, N. I., *Some Basic Problems of the Mathematical Theory of Elasticity*, 4th ed., Wolters-Noordhoff, Groningen, Netherlands, 1963.

Needleman, A., An analysis of intersonic crack growth under shear loading, *J. Appl. Mech.*, *66*, 847–857, 1999.

Olsen, K. B., R. Madariaga, and R. J. Archuleta, Three-dimensional dynamic simulation of the 1992 Landers earthquake, *Science*, *278*, 834–838, 1997.

Palmer, A. C., and J. R. Rice, The growth of slip surfaces in the progressive failure of over-consolidated clay, *Proc. R. Soc. London, Ser. A*, *332*, 527–548, 1973.

Perrin, G., J. R. Rice, and G. Zheng, Self-healing slip pulse on a frictional surface, *J. Mech. Phys. Solids*, *43*, 1461–1495, 1995.

Prakash, V., and R. J. Clifton, Pressure-shear plate impact measurement of dynamic friction for high speed machining applications, in *Proceedings of VII International Congress on Experimental Mechanics*, pp. 568–596, Soc. for Exp. Mech., Bethel, Conn., 1992.

Prakash, V., and R. J. Clifton, Time resolved dynamic friction measurements in pressure shear, in *Experimental Techniques in the Dynamics of Deformable Solids*, pp. 33–48, Am. Soc. of Mech. Eng., Appl. Mech. Div., New York, 1993.

Quin, H., Dynamic stress drop and rupture dynamics of the October 15, 1979 Imperial Valley earthquake, *Tectonophysics*, *175*, 93–117, 1990.

Ramulu, M., and A. S. Kobayashi, Mechanics of crack curving and branching—A dynamic fracture analysis, *Int. J. Fract.*, *27*, 187–201, 1985.

Ranjith, K., and J. R. Rice, Slip dynamics at an interface between dissimilar materials, *J. Mech. Phys. Solids*, *49*, 341–361, 2000.

Ravichandar, K., and W. G. Knauss, An experimental investigation into dynamic fracture, 2, Microstructural aspects, *Int. J. Fract.*, *26*, 65–80, 1984a.

Ravichandar, K., and W. G. Knauss, An experimental investigation into dynamic fracture, 3, On steady-state crack propagation and crack branching, *Int. J. Fract.*, *26*, 141–154, 1984b.

Rice, J. R., The mechanics of earthquake rupture, in *Physics of the Earth's Interior*, edited by E. Boschi, pp. 555–649, North-Holland, New York, 1980.

Rice, J. R., and A. L. Ruina, Stability of steady frictional slipping, *J. Appl. Mech.*, *50*, 343–349, 1983.

Rosakis, A. J., O. Samudrala, R. P. Singh, and A. Shukla, Intersonic crack propagation in bimaterial systems, *J. Mech. Phys. Solids*, *46*, 1789–1813, 1998.

Rosakis, A. J., O. Samudrala, and D. Coker, Cracks faster than the shear wave speed, *Science*, *284*, 1337–1340, 1999.

Rosakis, A. J., O. Samudrala, and D. Coker, Intersonic shear crack growth along weak planes, *Mater. Res. Innovations*, *3*, 236–243, 2000.

Ruina, A., Slip instability and state variable friction laws, *J. Geophys. Res.*, *88*, 10,359–10,370, 1983.

Scholz,, C. H., *The Mechanics of Earthquakes and Faulting*, Cambridge Univ. Press, New York, 1990.

Singh, R. P., J. Lambros, A. Shukla, and A. J. Rosakis, Investigation of the mechanics of intersonic crack propagation along a bimaterial interface using coherent gradient sensing and photoelasticity, *Proc. R. Soc. London, Ser. A*, *453*, 2649–2667, 1997.

Spudich, P., and E. Cranswick, Direct observation of rupture propagation during the 1979 Imperial Valley earthquake using a short baseline accelerometer array, *Bull. Seismol. Soc. Am.*, *74*, 2083–2114, 1984.

Washabaugh, P. D., and W. G. Knauss, A reconciliation of dynamic crack velocity and Rayleigh wave speed in isotropic brittle solids, *Int. J. Fract.*, *65*, 97–114, 1994.

Weertman, J., Unstable slippage across a fault that separates elastic media of different elastic constants, *J. Geophys. Res.*, *85*, 1455–1461, 1980.

Winkler, S., D. A. Shockey, and D. A. Curran, Crack propagation at supersonic velocities, I, *Int. J. Fract. Mech.*, *6*, 151–158, 1970.

Yu, H. H., and Z. Suo, Intersonic crack growth on an interface, *Proc. R. Soc. London, Ser. A*, *456*, 223–246, 2000.

Zheng, G., and J. R. Rice, Conditions under which velocity-weakening friction allows a self-healing versus a cracklike mode of rupture, *Bull. Seismol. Soc. Am.*, *88*, 1466–1483, 1998.

Y. Huang, Department of Mechanical and Industrial Engineering, University of Illinois at Urbana-Champaign, Urbana, IL 61801, USA. (huang9@uiuc.edu)

A. J. Rosakis and O. Samudrala, Graduate Aeronautical Laboratories, California Institute of Technology, Pasadena, CA 91125, USA. (rosakis@aero.caltech.edu)